

BEYOND FIRST-ORDER UPWINDING: THE ULTRA-SHARP ALTERNATIVE FOR NON-OSCILLATORY STEADY-STATE SIMULATION OF CONVECTION

B. P. LEONARD AND SIMIN MOKHTARI

Department of Mechanical Engineering, The University of Akron, OH 44325, U.S.A.

SUMMARY

Although it is now well known that first-order convection schemes suffer from serious inaccuracies attributable to artificial viscosity or numerical diffusion under high-convection conditions, these methods continue to enjoy widespread popularity for numerical heat-transfer calculations, apparently owing to a perceived lack of viable high-accuracy alternatives. But alternatives are available. For example, non-oscillatory methods used in gasdynamics, including currently popular 'TVD' schemes, can be easily adapted to multidimensional incompressible flow and convective transport. This, in itself, would be a major advance for numerical convective heat transfer, for example. But, as this paper shows, second-order TVD schemes form only a small, overly restrictive, subclass of a much more universal, and extremely simple, non-oscillatory flux-limiting strategy which can be applied to convection schemes of arbitrarily high-order accuracy, while requiring only a simple tridiagonal ADI line-solver, as used in the majority of general-purpose iterative codes for incompressible flow and numerical heat transfer. The new universal limiter and associated solution procedures form the so-called ULTRA-SHARP alternative for high-resolution non-oscillatory multidimensional steady-state high-speed convective modelling.

INTRODUCTION

For many years the state of the art in high-speed convective modelling, especially in the field of numerical heat and mass transfer, has been dominated by first-order upwinding, often in the guise of the 'Hybrid' scheme of Spalding¹ or, more recently, the related 'Power-Law Differencing Scheme' (PLDS) of Patankar.² This situation has clearly evolved from an attempt to remedy the infamous problems of unphysical oscillations and instabilities associated with 'classical' central-difference methods under high-convection conditions, using practical grids. The Hybrid scheme avoids oscillatory behaviour by switching from second-order central to first-order upwinding for convection (and omitting modelled physical diffusion) wherever the local component grid Peclet (or Reynolds) number exceeds a value of 2. PLDS and the exponential differencing scheme (EDS) on which it is based³ involve a more subtle blending strategy, but both are also equivalent to first-order upwinding for convection (with physical diffusion totally suppressed) for component grid Peclet numbers greater than about 6. For most cases of practical interest, especially in three dimensions where very fine meshes are out of the question, the actual (laminar or turbulent) component grid Peclet or Reynolds numbers are likely to be orders of magnitude larger than 2 or 6 throughout the bulk of the flow domain. This means that Hybrid and PLDS are operating as first-order upwinding almost everywhere in the flow-field except at a very small fraction of

grid-points near boundaries and stagnation regions where the convecting velocities are small. Thus, instead of solving a high-convection problem, these methods simulate an unphysical (and anisotropic) *low-convection* problem in which the effective local component grid Peclet or Reynolds number can never be greater than 2.

As has been well established theoretically for over a decade,⁴⁻⁶ first-order upwinding for convection is a highly inaccurate method because of the effects of global artificial numerical diffusion (or artificial viscosity). Thus, in many cases of practical interest, Hybrid or PLDS may give rather low-accuracy results; this has been directly confirmed in several comparative benchmark studies.⁷⁻¹⁰ Hybrid and PLDS, as used in various evolutions of the well-known TEACH code,¹¹ have been most successful for flows in which the convective terms are not important; i.e. for essentially potential flow governed by the kinematic constraint of the continuity equation ($\nabla \cdot \mathbf{v} = 0$), modified by boundary regions which are usually handled by built-in 'wall-functions', and for turbulence modelling when turbulent transport equations are dominated by source-sink terms.¹² However, for simulating recirculating flows or strong shear flows or for predicting scalar transport, these methods must be considered to be highly unreliable because of the inherent global artificial viscosity or diffusivity.

Even though these defects are well documented and generally acknowledged, the Hybrid and PLDS methods continue to enjoy widespread popularity, apparently because available alternatives claiming better accuracy (such as higher-order upwinding) are either not well known or have been discarded because of perceived incompatibilities with TEACH-like solution algorithms.¹⁰ When carefully applied to three-dimensional laminar recirculating flows, however, higher-order upwinding methods such as QUICK¹³ have been extremely successful,¹⁴ showing fine-scale details on relatively coarse grids that are simply wiped out by artificial numerical viscosity in the corresponding Hybrid calculation.¹⁵ In many convection-dominated flow problems, the multi-dimensional QUICK scheme has been shown to be stable, economical and highly accurate; because of the wider computational stencil, the solution algorithm is most naturally cast in pentadiagonal form,¹⁶ but can also be used with conventional tridiagonal solvers provided that 'outlying' and other compensating terms are carefully transferred to the source term.¹⁷

However, in some cases (such as turbulent flows, for example) there may be problems with higher-order upwinding because, in regions involving sudden jumps in value, there is a tendency for the simulation to overshoot or undershoot the correct transition value. In many cases, this presents no problem other than slight inaccuracy; however, in codes where turbulent transport variables (such as eddy viscosity, for example) are computed as part of the solution procedure, it is possible for a modelled transport coefficient to undershoot to a point where it takes on locally negative values, thus resulting in violent non-linear instability. Similar defects occur in various forms of skew upwinding.^{8,18} There have been recent attempts to suppress the undershoot problem by blending higher-order (or skew) upwinding methods with standard (component-wise) first-order upwinding, using sophisticated blending strategies.^{19,20} Although much more accurate than Hybrid or PLDS, these methods still generate an unnecessary degree of numerical smearing when attempting to simulate near-discontinuities.

The current situation in numerical gasdynamics is considerably better. The most popular schemes are based on second-order central differencing for all spatial derivatives, as used in the canonical second-order Lax-Wendroff method,²¹ for example, together with explicitly added global fourth-order artificial dissipation (a spatial fourth-difference term) to enhance convergence in smooth regions and an explicit *locally varying non-linear* solution-dependent artificial diffusivity or viscosity (a spatial second-difference term) to inhibit oscillations in regions of sharply varying gradient.^{22,23} This explicit damping of a potentially oscillatory scheme is usually quite

successful in giving second-order accuracy without excessive oscillation or gross artificial smearing. In general terms, Hybrid and PLDS could be considered to follow a similar philosophy: i.e. using second-order central differencing with locally varying solution-dependent artificial diffusivity or viscosity added explicitly. But a major difference lies in the strategy adopted for the evaluation of the *magnitude* of the artificial terms. With Hybrid and PLDS it is a function of the local component grid Peclet or Reynolds number, so that artificial diffusivity is always large wherever physical convection dominates physical diffusion at the grid-cell level, thus guaranteeing that *modelled* convection *never* dominates numerical diffusion. By contrast, the magnitude of the gasdynamic codes' artificial diffusivity depends in a non-linear way on local behaviour of the convected field variables: very low in smooth regions, but rapidly increasing in regions of strongly varying gradients (high curvature), irrespective of the local Reynolds number, which could be infinite (as in Euler-equation simulations). Thus, in these schemes, artificial viscosity is explicitly added (automatically) only where 'needed' (to suppress potential oscillations near shock waves or contact discontinuities, for example). This technique has been developed into a sophisticated art with so-called 'shock-capturing' and 'total-variation-diminishing' (TVD) schemes,^{24,25} which may even involve local *negative* artificial viscosity, resulting in 'artificial compression' to aid in numerically steepening discontinuities without overshoot. The popular 'Superbee' scheme is of this latter type.²⁶

Apparently there has never been any attempt to explicitly adapt the highly successful second-order gasdynamic codes or the so-called 'high-resolution' (but formally still second-order) TVD schemes to incompressible flows and convective heat and mass transfer, even though (as will be shown) this is extremely simple to do, using either explicit time-marching or an iterative pentadiagonal matrix algorithm based on a variable-curvature-factor technique.^{27,28} But it turns out that the commonly used TVD flux limiters form an overly restrictive subclass of a much more universal technique guaranteeing tight resolution of discontinuities without overshoots or undershoots; and this 'universal limiter' can be applied to methods of arbitrarily high-order accuracy, giving very sharp resolution without introducing artificial numerical compression (and concomitant distortion and clipping of smooth profiles²⁹). The strategy developed here is based on a simple high-accuracy resolution program which uses third-order upwinding in smooth regions and adaptively increases the accuracy (by locally expanding the computational stencil automatically) in high-curvature regions, while applying the universal limiter to eliminate any possibility of overshoot or oscillation. Thus, the Universal Limiter for Tight Resolution and Accuracy in combination with this Simple High-Accuracy Resolution Program results in the 'ULTRA-SHARP' alternative for high-speed non-oscillatory steady-state convective modelling.

In the next section, the primary shortcomings of Hybrid and PLDS are briefly reviewed. Also, the undershoot (overshoot) problems of higher-order upwinding are demonstrated. The subsequent section describes the Normalized Variable Diagram (NVD), the construction of the universal limiter and its implicit implementation via the Downwind Weighting Factor (DWF). The DWF has the added advantage of converting an arbitrarily high-order scheme in N dimensions (using a correspondingly wide stencil) into a compact $(2N + 1)$ -point scheme involving only scalar *tridiagonal* ADI solution methods, thus making the ULTRA-SHARP strategy immediately available for incorporation into TDMA-based TEACH-type codes. Some of the more popular TVD schemes are also described within the framework of the NVD and in terms of the Variable Curvature Factor (VCF) which is most naturally used with a pentadiagonal solver.²⁷ Finally, the performance of the ULTRA-SHARP alternative is demonstrated on a number of simple two-dimensional steady-state benchmark test problems for scalar transport in prescribed velocity fields.

SHORTCOMINGS OF HYBRID AND PLDS

Effective grid Peclet number

Consider the model convection–diffusion equation in one dimension for a scalar Φ ,

$$\frac{\partial \Phi}{\partial t} = -u \frac{\partial \Phi}{\partial x} + D \frac{\partial^2 \Phi}{\partial x^2} \quad (1)$$

for constant (positive) u and D . The forward-time, central-space (FTCS) discretization of this equation takes the form³⁰

$$\frac{\Phi_i^{n+1} - \Phi_i^n}{\Delta t} = -u \frac{(\Phi_{i+1}^n - \Phi_{i-1}^n)}{2\Delta x} + D \frac{(\Phi_{i+1}^n - 2\Phi_i^n + \Phi_{i-1}^n)}{\Delta x^2} \quad (2)$$

using standard index notation on a uniform grid. This can be rearranged as

$$\Phi_i^{n+1} = \Phi_i^n - \frac{c}{2}(\Phi_{i+1}^n - \Phi_{i-1}^n) + \frac{|c|}{P_\Delta}(\Phi_{i+1}^n - 2\Phi_i^n + \Phi_{i-1}^n) \quad (3)$$

introducing the Courant number

$$c = u\Delta t/\Delta x \quad (4)$$

and the cell Peclet number (or Reynolds number, in the case of momentum or vorticity transport).

$$P_\Delta = |u|\Delta x/D \quad (5)$$

Equation (1) can also be discretized using first-order upwinding for the convection term and simply ignoring the physical diffusion term, giving (for $u > 0$)

$$\Phi_i^{n+1} = \Phi_i^n - c(\Phi_i^n - \Phi_{i-1}^n) \quad (6)$$

with a similar form for $u < 0$. Equation (6) can be rewritten in the form of equation (3) as

$$\Phi_i^{n+1} = \Phi_i^n - \frac{c}{2}(\Phi_{i+1}^n - \Phi_{i-1}^n) + \frac{|c|}{P_\Delta^*}(\Phi_{i+1}^n - 2\Phi_i^n + \Phi_{i-1}^n) \quad (7)$$

where the effective grid Peclet number is, in this case,

$$P_\Delta^* \equiv 2 \quad (8)$$

Thus, the Hybrid scheme—using equation (3) for $P_\Delta \leq 2$ and equation (6) for $P_\Delta > 2$ —can be written in the form of equation (7) with

$$P_\Delta^* = P_\Delta \quad \text{for} \quad P_\Delta \leq 2 \quad (9)$$

and

$$P_\Delta^* \equiv 2 \quad \text{for} \quad P_\Delta > 2 \quad (10)$$

Now consider an exact solution of the *steady-state* form of equation (1) with a downstream boundary condition $\Phi(L) = 1$, and with $\Phi = 0$ far upstream. This can be written

$$\Phi(x) = \exp[-(L-x)/\lambda] \quad \text{for} \quad x \leq L \quad (11)$$

where the length-constant λ is given by

$$\lambda = D/u \quad (12)$$

The corresponding central-difference equation is

$$(2 - P_\Delta)\Phi_{i+1} - 4\Phi_i + (2 + P_\Delta)\Phi_{i-1} = 0 \quad (13)$$

and the *analytical* solution of this difference equation for the above boundary conditions is

$$\Phi_k = \left(\frac{2 - P_\Delta}{2 + P_\Delta} \right)^k \quad (14)$$

where k is an integer defined, for discrete values of x , by

$$k = (L - x)/\Delta x \quad \text{for } x \leq L \quad (15)$$

Note that the exact solution of the differential equation, equation (11), can be written, for discrete node values, as

$$\Phi_k = (e^{-P_\Delta})^k \quad (16)$$

Thus, for $P_\Delta < 2$, the central-difference solution is like a solution to the differential equation, but at a larger grid Peclet number. And for $P_\Delta > 2$, equation (14) shows that the discrete solution becomes oscillatory, as is well known.³⁰ These features are demonstrated in Figure 1, which shows the factors in equations (14) and (16) as a function of P_Δ .

Now consider equation (13) rewritten in terms of an *effective* grid Peclet number, P_Δ^* :

$$(2 - P_\Delta^*)\Phi_{i+1} - 4\Phi_i + (2 + P_\Delta^*)\Phi_{i-1} = 0 \quad (17)$$

The solution of this equation is of the same form as equation (14), with P_Δ replaced by P_Δ^* . But this can be forced to match the true solution, equation (16), by setting

$$\frac{2 - P_\Delta^*}{2 + P_\Delta^*} = e^{-P_\Delta} \quad (18)$$

giving, on rearrangement, an explicit formula for the effective grid Peclet number in terms of the

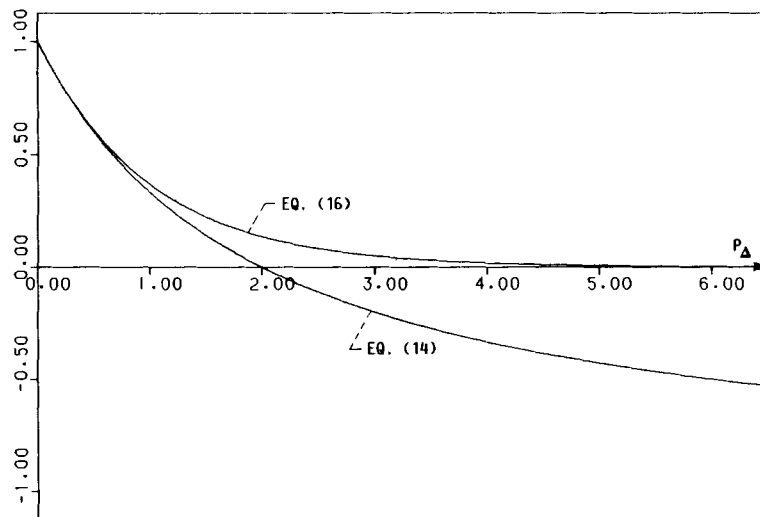


Figure 1. Algebraic and exponential factors appearing in equations (14) and (16), respectively, as a function of grid Peclet number, P_Δ

physical value

$$P_{\Delta}^* = 2 \tanh(P_{\Delta}/2) \quad (19)$$

This is the basis of the exponential difference scheme³ or so-called 'optimal' upwinding.^{3,1} Using P_{Δ} -dependent weighting factors for convection and diffusion, Raithby and Schneider³ develop algebraic approximations (to avoid expensive exponential evaluations) which can easily be shown to be equivalent to an approximation to equation (19) given by

$$P_{\Delta}^*(R \& S) = \left[\frac{P_{\Delta}^2}{2(5 + P_{\Delta}^2)} + \frac{(1 + 0.005 P_{\Delta}^2)}{P_{\Delta}(1 + 0.05 P_{\Delta}^2)} \right]^{-1} \quad (20)$$

for all (positive) values of P_{Δ} . Similarly, Patankar's power-law scheme² can be interpreted as

$$P_{\Delta}^*(PLDS) = \left. \begin{aligned} &\frac{2P_{\Delta}}{P_{\Delta} + 2(1 - 0.1P_{\Delta})^5} && 0 \leq P_{\Delta} \leq 10 \\ &= 2 && P_{\Delta} > 10 \end{aligned} \right\} \quad (21)$$

In the same spirit, Spalding's Hybrid scheme,¹ given by equations (9) and (10), could be interpreted as a (much less accurate) piecewise linear approximation of the hyperbolic-tangent function. Equations (9) and (10), (19), (20) and (21) are portrayed in Figure 2. As defined, Hybrid is equivalent to first-order upwinding for convection with physical diffusion omitted (i.e. $P_{\Delta}^* = 2$) for $P_{\Delta} > 2$. But also note that the other schemes are effectively equivalent to this for P_{Δ} greater than about 6. This is an important point which is sometimes lost in the details of the algebraic or power-law approximations. In other words, although (as seen from Figure 2) equations (20) and (21) are both very good engineering approximations to the tanh curve, the exponential difference scheme itself is equivalent to *first-order upwinding for convection with physical diffusion switched off*, for physical grid Peclet numbers larger than about 6. This, of course, is entirely appropriate for the model physical problem on which equation (19) is based; for $P_{\Delta} > 6$, the solution is essentially a constant ($\Phi = 0$) at all computed points, since the effect of the downstream boundary condition does not diffuse upstream strongly enough to significantly affect the nearest computed point (e.g. $e^{-6} \approx 0.25$ per cent). But this (steady, source-free, one-dimensional, convection-diffusion) model problem is clearly very restrictive. For this reason, it is dangerous to use equation

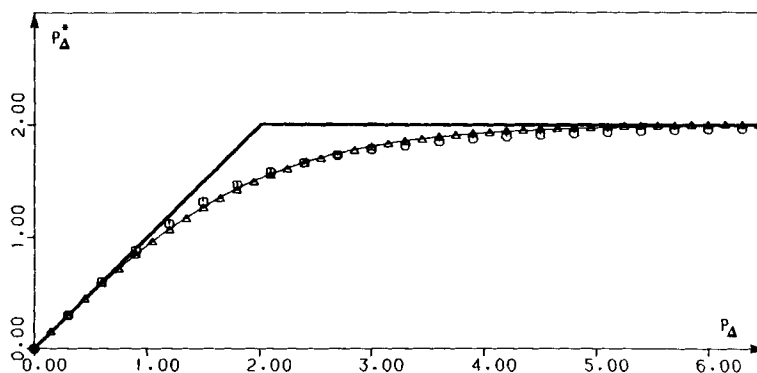


Figure 2. Approximations of the hyperbolic-tangent function given by equation (19). Exact curve: light continuous line. Hybrid: heavy piecewise linear approximation. Patankar power-law approximation: triangles. Raithby-and-Schneider algebraic approximation: circles

(19), or various equivalent formulations, as a basis for a general-purpose computational-fluid-dynamics algorithm. This is clearly demonstrated in the following section.

Source terms, multidimensionality and transients

To the extent that the fluid-dynamic problem being modelled differs from equation (1), Hybrid and PLDS (or EDS) introduce inaccuracies owing to the inherent artificial diffusion—for $P_\Delta > 2$ in the case of Hybrid, and for all P_Δ values for PLDS. For example, the introduction of a source term into equation (1), representing either a real source term in one dimension or the effects of transverse transport in a multidimensional flow, results in a serious degradation in accuracy when these methods are used. Figure 3 shows a steady-state two-point boundary-value problem

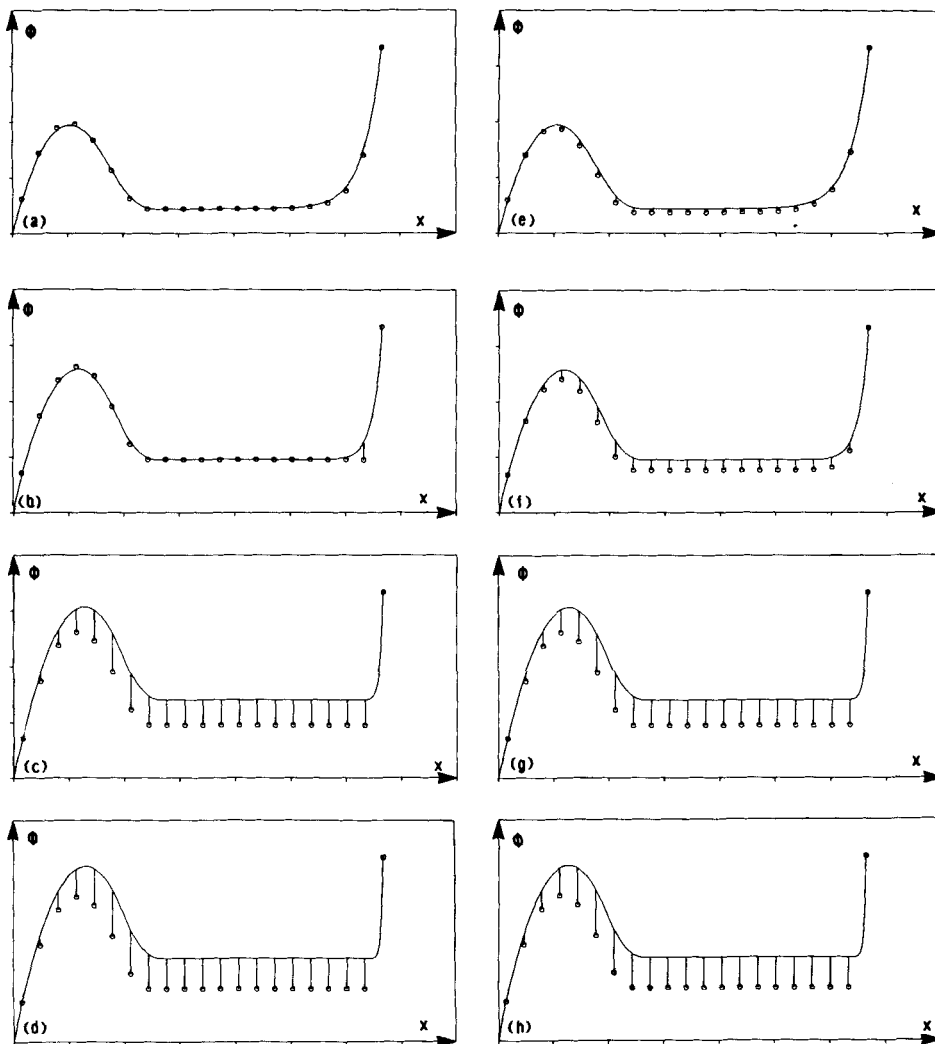


Figure 3. Steady-state boundary-value problem with source term given by equation (23). Hybrid method for: (a) $P_\Delta = 1$; (b) $P_\Delta = 2$; (c) $P_\Delta = 6$; (d) $P_\Delta = 10$. PLDS method for: (e) $P_\Delta = 1$; (f) $P_\Delta = 2$; (g) $P_\Delta = 6$; (h) $P_\Delta = 10$

corresponding to the model equation

$$u \frac{\partial \Phi}{\partial x} = D \frac{\partial^2 \Phi}{\partial x^2} + S(x) \quad (22)$$

using a piecewise linear source term given by⁷

$$\left. \begin{aligned} S(x) &= 10 - 50i\Delta x & \text{for } i\Delta x \leq 0.3 \\ S(x) &= 50i\Delta x - 20 & \text{for } 0.3 \leq i\Delta x \leq 0.4 \\ S(x) &= 0 & \text{for } i\Delta x \geq 0.4 \end{aligned} \right\} \quad (23)$$

where i is a grid-index measured from the left-hand end and $x = i\Delta x$. Solutions are shown using both Hybrid and PLDS for $P_\Delta = 1, 2, 6$ and 10 . Note that, for $P_\Delta = 1$ and 2 , Hybrid (operating as second-order central differencing) gives adequate solutions; but PLDS is already clearly in error even at these small P_Δ values. Clearly, for $P_\Delta > 2$, the Hybrid solution does not change, since the effective P_Δ^* is frozen at 2 . With PLDS, the corresponding 'saturated' solution occurs at about $P_\Delta = 6$, corresponding to Figure 2. Note that this is due to the shape of the hyperbolic-tangent function and has nothing to do with any errors involved in the power-law approximation of \tanh .

To demonstrate the effects of multidimensionality, Figure 4 shows the well-known oblique-step test, corresponding to steady two-dimensional convection and diffusion governed by the model equation.

$$u \frac{\partial \Phi}{\partial x} + v \frac{\partial \Phi}{\partial y} = D \left(\frac{\partial^2 \Phi}{\partial x^2} + \frac{\partial^2 \Phi}{\partial y^2} \right) \quad (24)$$

with a constant convecting velocity, $\mathbf{v} = (u, v)$, at an angle θ to the (uniform square) grid, and a prescribed unit-step jump in Φ on the upstream boundary. As θ is varied, the position of the boundary jump is adjusted so that the centreline of the transition passes through the centre-point of the grid. Figure 5 shows analytical solutions³² for $P_\Delta (= |\mathbf{v}|\Delta x/D) = 100$, at $\theta = 30^\circ, 45^\circ$ and 60° . The analytical solution omits streamwise diffusion and is therefore valid only at moderate-to-high P_Δ values.³³ At this grid Peclet number, both Hybrid and PLDS are operating as pure

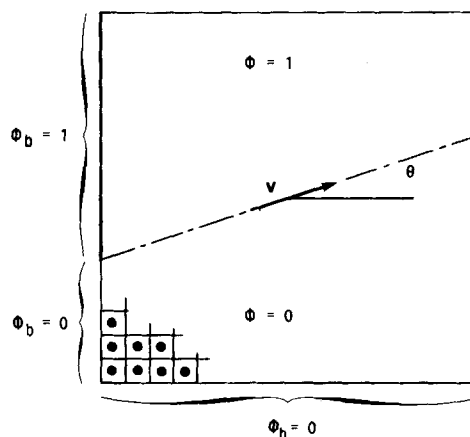


Figure 4. Schematic portrayal of the oblique-step test. As θ is varied, the location of the boundary discontinuity is adjusted so that the centreline of the transition passes through the midpoint of the grid

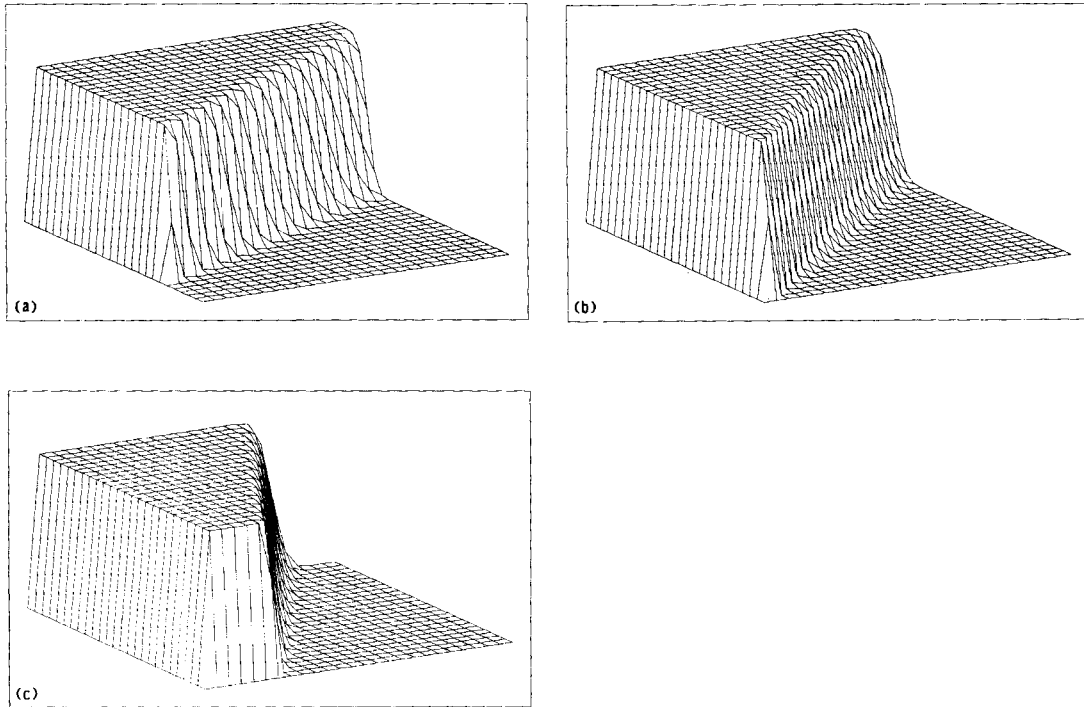


Figure 5. Three-dimensional plot of $\Phi(x, y)$ for the analytical solution of the oblique-step problem for $P_\Delta (= |\mathbf{v}|\Delta x/D) = 100$ and (a) $\theta = 30^\circ$, (b) $\theta = 45^\circ$ and (c) $\theta = 60^\circ$

first-order upwinding for convection with physical diffusion omitted. As seen in Figure 6, this results in gross artificial diffusion in a direction transverse to the flow—a well-known phenomenon.⁴ Note the large absolute error, given by

$$\mathcal{E} = \sum_i \sum_j |\Phi_{\text{comp}} - \Phi_{\text{exact}}| \quad (25)$$

summed over all computed grid-points on a 25×25 square mesh. The effects of varying θ (by 1° increments) are summarized in Figure 7. Note the symmetry with respect to $\theta = 45^\circ$, where there is a slight drop in error due to alignment across diagonal nodes; other undulations are due to similar interactions between the almost-discontinuous exact profile and the discrete nodal points, as the angle is varied. Clearly, except when the direction of the convecting velocity is closely aligned with the grid ($\theta \rightarrow 0^\circ, 90^\circ, \dots$), the artificial diffusion of these methods at practical (i.e. large) grid Peclet numbers results once again in highly inaccurate predictions.

Finally, Figure 8 shows results of simulating the transient pure-convection equation (for $u = \text{const} > 0$)

$$\frac{\partial \Phi}{\partial t} + u \frac{\partial \Phi}{\partial x} = 0 \quad (26)$$

for an isolated sine-squared profile $20\Delta x$ wide (representing a 'smooth' function) and a unit step, using Hybrid or PLDS (or EDS)—equivalent to pure first-order upwinding for this infinite- P_Δ case—and an explicit forward time-step, i.e.

$$\Phi_i^{n+1} = \Phi_i^n - c(\Phi_i^n - \Phi_{i-1}^n) \quad (27)$$

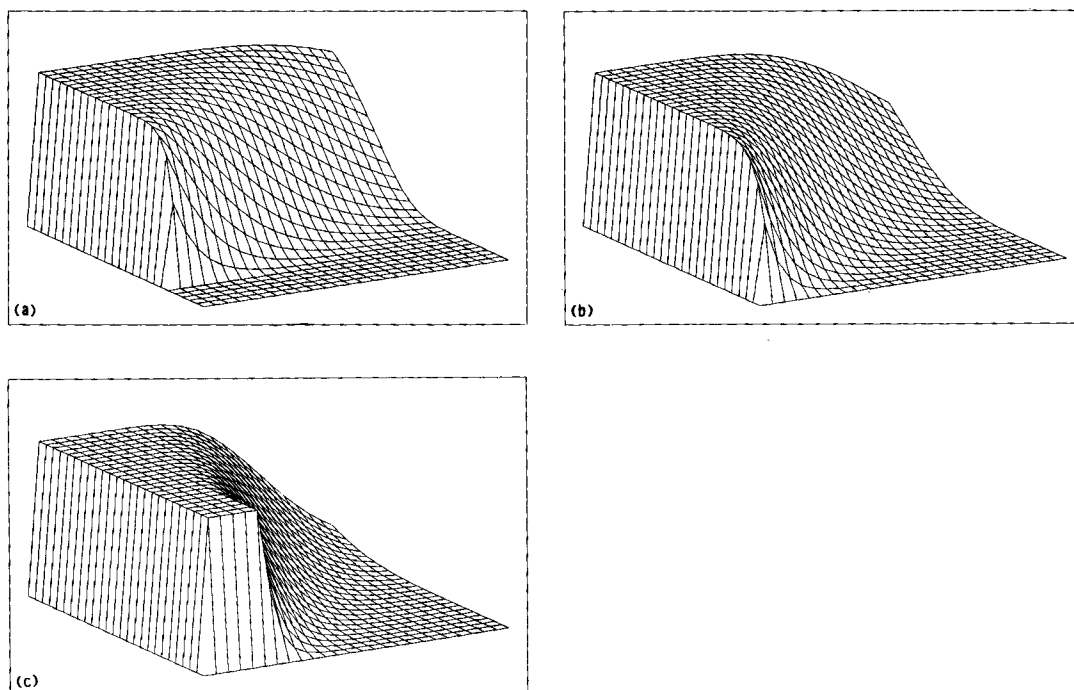


Figure 6. Corresponding solution of the oblique-step problem using first-order upwinding—equivalent to Hybrid, PLDS or EDS at this Peclet number ($P_\Delta = 100$): (a) $\theta = 30^\circ$, $\mathcal{E} = 50.6$; (b) $\theta = 45^\circ$, $\mathcal{E} = 64.2$; (c) $\theta = 60^\circ$, $\mathcal{E} = 50.6$. \mathcal{E} is defined in equation (25)

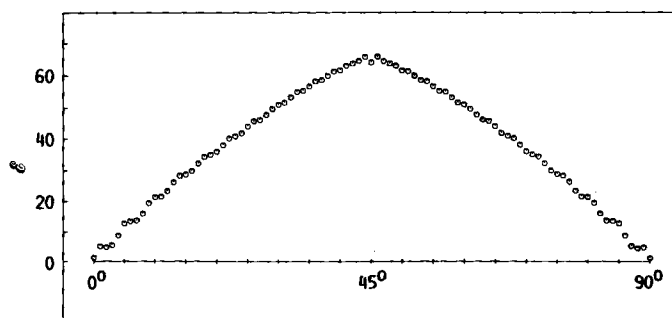


Figure 7. Variation of total absolute error, \mathcal{E} , with stream-to-grid angle, θ , in 1° increments for PLDS at $P_\Delta = 100$ (equivalent to first-order upwinding except near 0° and 90°). Maximum \mathcal{E} is 65.9 at 44° or 46°

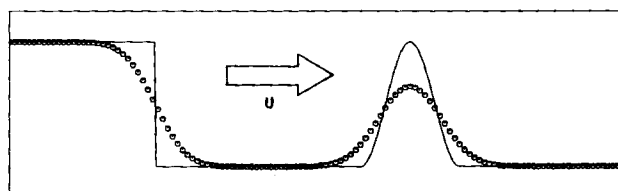


Figure 8. First-order-upwind solution of the inviscid transient convection problem for a unit step and an isolated sine-squared profile, after 100 time-steps at $c = 0.45$

At the time shown, the exact profiles have moved 45 mesh-widths to the right. Starting from exact initial conditions, the computed results again demonstrate the gross artificial diffusion corresponding, in the transient case, to a numerical diffusion coefficient of the form³⁰

$$D_{\text{num}} = u\Delta x(1 - c)/2 \quad (28)$$

In the case shown, $c = 0.45$; from equation (28), numerical diffusion is clearly worse at smaller Courant numbers.

As the above simple test cases show, Hybrid and PLDS are essentially equivalent to first-order upwinding of convection with physical diffusion ignored for grid Peclet numbers larger than 2 or about 6, respectively. This must cast serious doubt on the reliability of simulations using these methods for complex high-speed multidimensional flows using practical (i.e. relatively coarse) meshes. In addition, it seems to make no sense to use sophisticated (and expensive) multiple-equation turbulence models with these convection schemes—as is usually done—because wherever the computed (turbulent) component grid Peclet (or Reynolds) number exceeds 2 (Hybrid) or 6 (PLDS), the turbulent transport terms are (actually or effectively) omitted from the momentum and scalar transport equations (and from the turbulent transport equations themselves)—having been replaced by the artificial numerical diffusion inherent in the truncation error of the modelled convection terms. Apart from the questionable logic involved, one wonders how turbulence modelling itself has been affected by such convection methods—since, except as an expensive diagnostic to switch itself off, turbulent transport is largely ignored in most of the flow domain (except near solid boundaries where universal wall-functions are used anyway).

PROBLEMS WITH HIGHER-ORDER METHODS

Spurious oscillation of symmetrical schemes

Although the artificial diffusion associated with Hybrid and PLDS is widely acknowledged and well documented, these methods continue to enjoy widespread popularity.³⁴ This appears to be because simple alternatives, with formally higher-order accuracy, introduce other anomalies—usually in the form of overshoots, undershoots or severe oscillations—which may lead to convergence problems or non-linear instability. The primary motivation for Hybrid and PLDS seems to be associated with the suppression of deeply penetrating oscillations which occur with ‘classical’ second-order central differencing for $P_\Delta > 2$, as discussed in relation to equation (14). Figure 9(a) shows the one-dimensional source-term boundary-value problem, considered earlier, at $P_\Delta = 10$ solved using second-order central differencing. As seen, the oscillations penetrate from the downstream boundary well into the solution domain. In fact, the penetration distance is directly proportional to P_Δ .⁷

By contrast, second-order upwinding for convection,³⁰ together with second-order central differencing for diffusion, written in control-volume (CV) form (for $u > 0$)

$$\begin{aligned} \frac{u}{\Delta x} \left\{ \left[\frac{1}{2}(\Phi_{i+1} + \Phi_i) - \frac{1}{2}(\Phi_{i+1} - 2\Phi_i + \Phi_{i-1}) \right] - \left[\frac{1}{2}(\Phi_i + \Phi_{i-1}) - \frac{1}{2}(\Phi_i - 2\Phi_{i-1} + \Phi_{i-2}) \right] \right\} \\ - \frac{D}{\Delta x^2} [(\Phi_{i+1} - \Phi_i) - (\Phi_i - \Phi_{i-1})] = S(x) \end{aligned} \quad (29)$$

where S is the CV average, gives non-oscillatory results for this one-dimensional problem, as seen in Figure 9(b) for $P_\Delta = 10$. This method also gives much better accuracy than Hybrid or PLDS; compare with Figures 3(d) and 3(h). This may seem to be a simple viable higher-order alternative

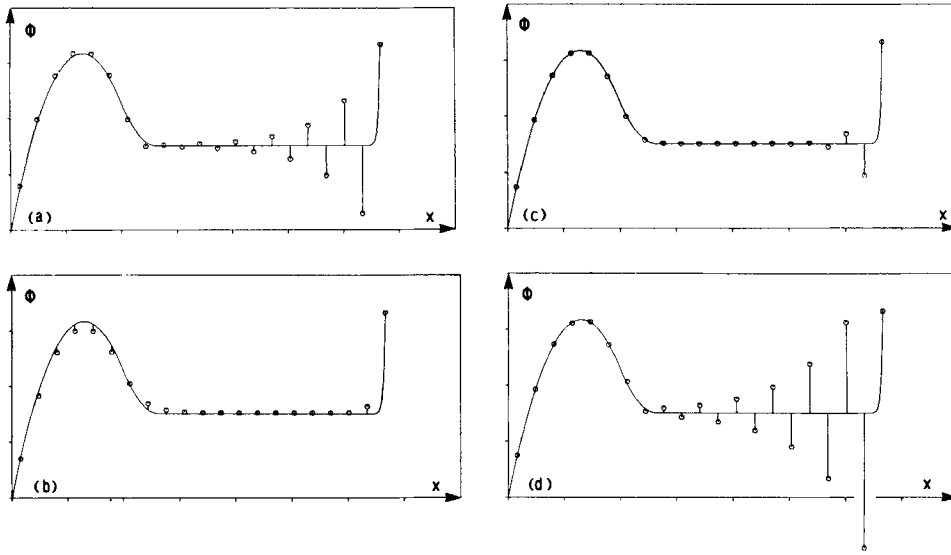


Figure 9. The steady source-term boundary-value problem of Figure 3 for $P_\Delta = 10$, using: (a) second-order central differencing; (b) second-order upwinding; (c) QUICK; (d) fourth-order central differencing

and has, in fact, been adopted as the basis for several codes, both incompressible³⁵ and compressible.³⁶ However, severe undershoot and overshoot problems develop when using second-order upwinding in two-dimensional computations, as will be shown.

Figure 9(c) shows the same one-dimensional problem solved by the QUICK method,³⁷ or third-order upwinding, which, being a control-volume formulation, takes the form (for $u > 0$)

$$\frac{u}{\Delta x} \left\{ \left[\frac{1}{2}(\Phi_{i+1} + \Phi_i) - \frac{1}{8}(\Phi_{i+1} - 2\Phi_i + \Phi_{i-1}) \right] - \left[\frac{1}{2}(\Phi_i + \Phi_{i-1}) - \frac{1}{8}(\Phi_i - 2\Phi_{i-1} + \Phi_{i-2}) \right] \right\} - \frac{D}{\Delta x^2} [(\Phi_{i+1} - \Phi_i) - (\Phi_i - \Phi_{i-1})] = S(x) \quad (30)$$

Typically, a few oscillations are generated near the downstream boundary jump. But the penetration distance does not continue to grow with P_Δ ; instead, it saturates at about $5\Delta x$ as $P_\Delta \rightarrow \infty$.³⁷ Note the much better (third-order) accuracy in the source-term region. There has been some confusion in the literature concerning the third-order accuracy of QUICK for convection; this is explained in Appendix I.

Many researchers appear to have an unsubstantiated aversion to unsymmetrical higher-order (upwind) methods, and prefer to work instead with higher-order *central* differencing. For example, the fourth-order central discretization in control-volume form is given by

$$\begin{aligned} \frac{u}{\Delta x} \left\{ \left[\frac{1}{2}(\Phi_{i+1} + \Phi_i) - \frac{1}{16}(\Phi_{i+2} - \Phi_{i+1} - \Phi_i + \Phi_{i-1}) \right] - \left[\frac{1}{2}(\Phi_i + \Phi_{i-1}) - \frac{1}{16}(\Phi_{i+1} - \Phi_i - \Phi_{i-1} + \Phi_{i-2}) \right] \right\} \\ - \frac{D}{\Delta x^2} \left\{ \left[(\Phi_{i+1} - \Phi_i) - \frac{1}{24}(\Phi_{i+2} - 3\Phi_{i+1} + 3\Phi_i - \Phi_{i-1}) \right] - \left[(\Phi_i - \Phi_{i-1}) - \frac{1}{24}(\Phi_{i+1} - 3\Phi_i + 3\Phi_{i-1} - \Phi_{i-2}) \right] \right\} = S(x) \quad (31) \end{aligned}$$

But, as seen in Figure 9(d), although the smooth-region accuracy is good, the downstream oscillation problem is actually *worse* than second order! Once again, penetration distance is proportional to P_Δ . This is a characteristic of all higher-order central-difference schemes; the proportionality constant actually *increases* with the formal order of accuracy.³⁸ From this simple test, it is seen why central differencing (of any order) is difficult to work with. At this point, second- and third- (and possibly higher) order *upwind* methods seem to offer better alternatives in terms of accuracy and stability.

Non-monotonicity of higher-order multidimensional upwinding

To demonstrate multidimensional effects, Figures 10 and 11 show second-order upwind and QUICK-2D¹³ solutions, respectively, of the oblique-step test for $P_\Delta = 100$, to be compared with the analytical and first-order solutions of Figures 5 and 6. Figure 10 clearly demonstrates the large undershoot and overshoot problems of second-order upwinding; but note the decrease in error from that of first-order upwinding (= Hybrid = PLDS). At 45° , QUICK gives qualitatively similar results to those of second-order upwinding, but with slightly *less* undershoot and overshoot and *steeper* resolution corresponding to the higher-order accuracy, as reflected by the smaller absolute error. Note the inverse relationship of undershoot and overshoot between these two methods as θ is varied. Figure 12 shows the angular variation (in 1° increments) of absolute

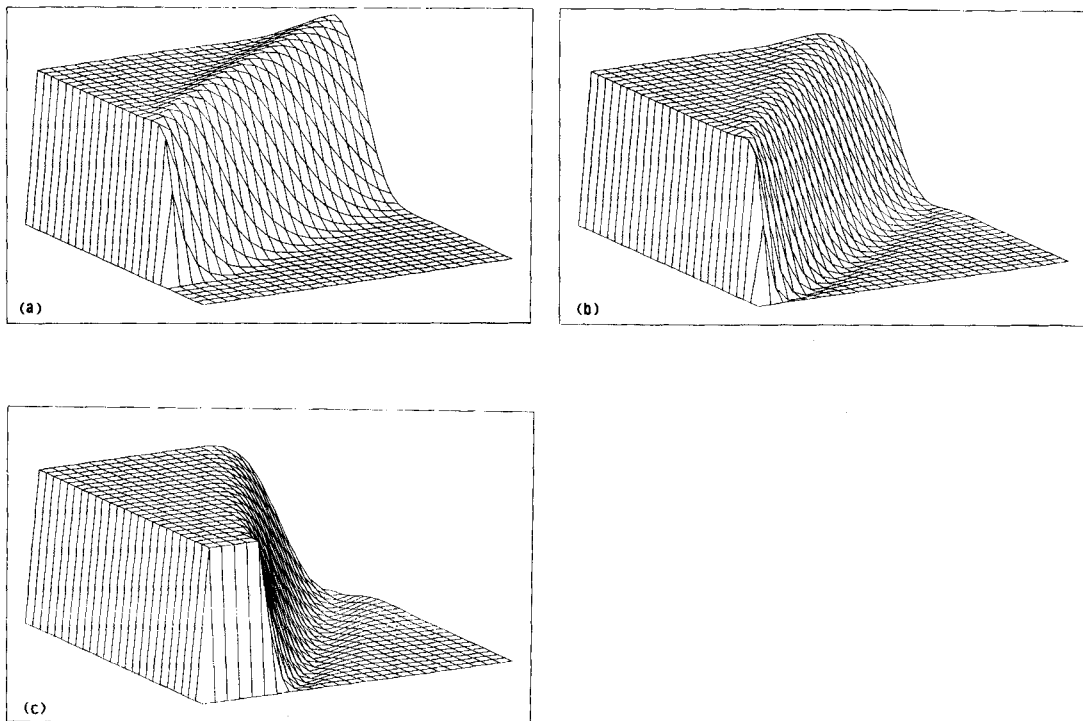


Figure 10. Results of the oblique-step problem for $P_\Delta = 100$ using second-order upwinding: (a) $\theta = 30^\circ$, $\mathcal{E} = 21.2$; (b) $\theta = 45^\circ$, $\mathcal{E} = 19.3$; (c) $\theta = 60^\circ$, $\mathcal{E} = 21.2$

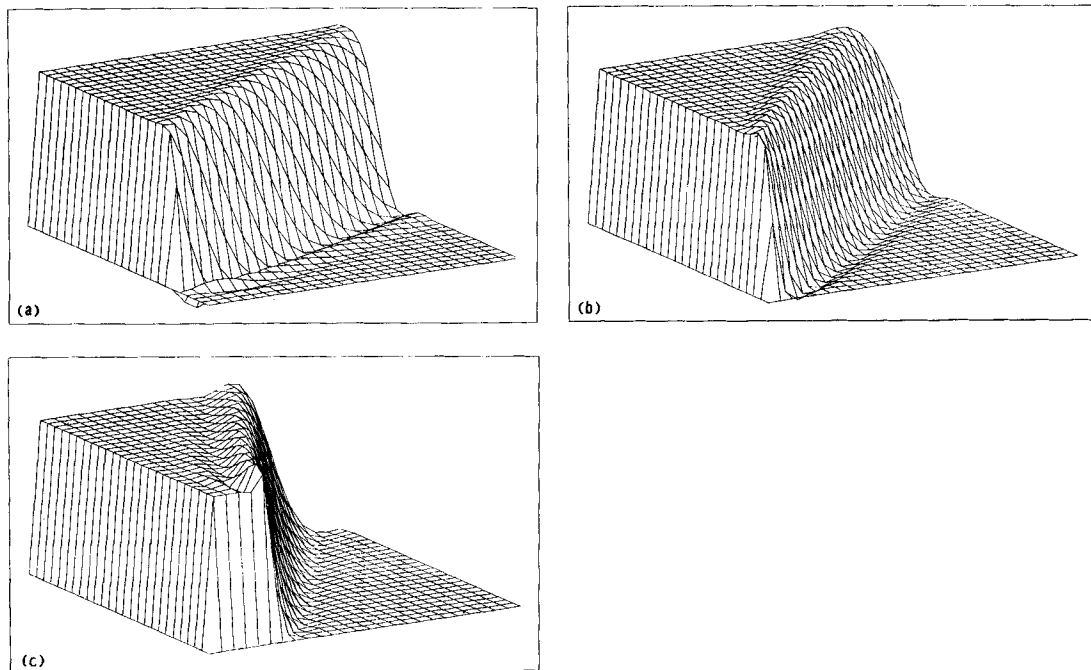


Figure 11. Results of the oblique-step problem for $P_{\Delta} = 100$ using QUICK-2D: (a) $\theta = 30^{\circ}$, $\mathcal{E} = 13.8$; (b) $\theta = 45^{\circ}$, $\mathcal{E} = 11.5$; (c) $\theta = 60^{\circ}$, $\mathcal{E} = 13.8$

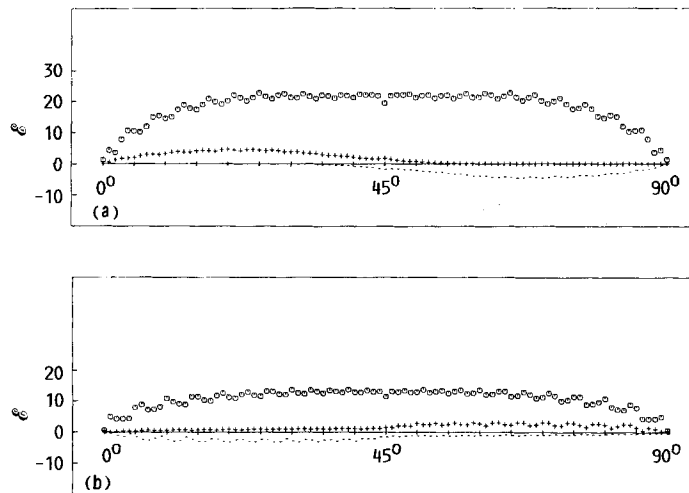


Figure 12. Angular variation of absolute error, \mathcal{E} , at $P_{\Delta} = 100$ for: (a) second-order upwinding (maximum = 22.5 at 25° or 65°); (b) QUICK-2D (maximum = 13.8 at 30° or 60°). Undershoots are shown by minus signs. Overshoots are shown by plus signs

error (at $P_{\Delta} = 100$) for both methods; cumulative contributions less than zero (undershoots) or greater than one (overshoots) are also shown; note the asymmetry between overshoots and undershoots—i.e. an overshoot at θ becomes an undershoot at $(90^{\circ} - \theta)$ and *vice versa*, in each case. Again, note the drop in error at 45° and the undular behaviour at other angles. The

two-dimensional oblique-step-test results of this and the previous section have been obtained by explicit time-marching to steady state; the conservative CV explicit flux formulation is summarized in Appendix II.

This simple test problem clearly demonstrates the non-monotonicity problems associated with higher-order methods in their 'unlimited' form. What is needed is a simple limiting strategy which maintains the good resolution of higher-order upwinding while eliminating undershoots and overshoots without introducing artificial diffusion or destroying conservation. The next section shows how this can be achieved in a straightforward manner using an extremely simple technique which can be extended to arbitrarily high-order accuracy.

THE ULTRA-SHARP ALTERNATIVE

Normalized variable diagram for the universal limiter

Figure 13 shows the local behaviour of the convected variable, $\Phi(x, y, z)$, in the vicinity of a control-volume (CV) face, in a direction normal to that face. Depending on the direction of the convecting velocity (here shown to the right), label the three indicated node values: Φ_D (down-wind), Φ_U (upwind) and Φ_C (centrally located between the other two), as shown. In part (a) of the figure, local behaviour is monotonic. One necessary condition of the universal limiter is sketched in the figure, shown by the cross-hatched limits: the convected face-value, Φ_f , should lie between adjacent node-values in locally monotonic regions. Note that this includes the limiting case, $\Phi_C = \Phi_D (= \Phi_f)$. But if $\Phi_C = \Phi_U$, an additional condition is necessary, namely: $\Phi_f = \Phi_C (= \Phi_U)$,

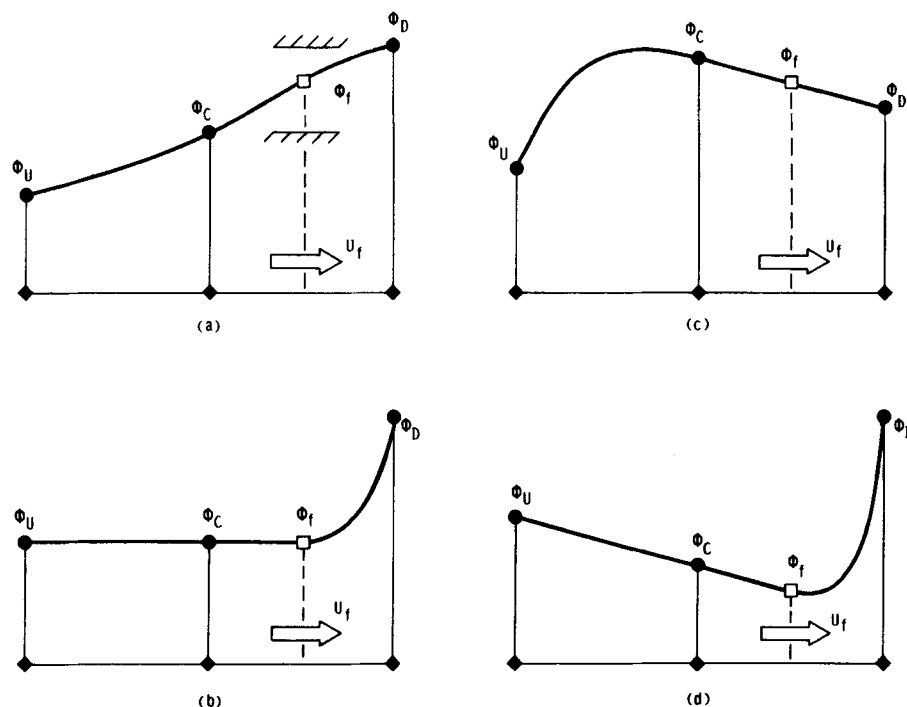


Figure 13. Convected face variable, Φ_f , depending on the local behaviour of Φ normal to the CV face: (a) locally monotonic; (b) $\Phi_C = \Phi_U$; (c) $\Phi_C > \Phi_D$; (d) $\Phi_C < \Phi_U$

in this case, as shown in part (b) of the figure. Treatment of locally non-monotonic behaviour is sketched in parts (c) and (d) of Figure 13. Some flexibility is possible here, provided the interpolation is consistent, in terms of continuity, with the previous conditions.

It is more convenient to summarize the limiter constraints in terms of *normalized variables*. Figure 14(a) shows local behaviour near a CV face in a direction normal to the face. Note that node-value labelling again conforms to the convecting velocity direction—in this case, to the left. Now define the normalized variable, $\tilde{\Phi}$, anywhere in the vicinity of this CV face as

$$\tilde{\Phi}(x, y, z) = \frac{\Phi(x, y, z) - \Phi_U}{\Phi_D - \Phi_U} \quad (32)$$

Note, in particular, that $\tilde{\Phi}_U = 0$ and $\tilde{\Phi}_D = 1$. Figure 14(b) gives the same information as 14(a), but in terms of normalized variables. Now the universal limiter constraints can be portrayed in the *Normalized Variable Diagram* (NVD)—i.e. the $(\tilde{\Phi}_C, \tilde{\Phi}_f)$ plane. This is shown in Figure 15. Symbolically, the universal limiter constraints on $\tilde{\Phi}_f$ can be written

$$\tilde{\Phi}_C \leq \tilde{\Phi}_f \leq 1 \quad \text{for } 0 < \tilde{\Phi}_C \leq 1 \quad (33)$$

with

$$\tilde{\Phi}_f = 0 \quad \text{at} \quad \tilde{\Phi}_C = 0 \quad (34)$$

and with continuous extensions beyond $\tilde{\Phi}_C > 1$ and $\tilde{\Phi}_C < 0$, maintaining a monotonically rising condition: $\partial \tilde{\Phi}_f / \partial \tilde{\Phi}_C > 0$. In Figure 15, these extensions are given by second-order central differencing for $\tilde{\Phi}_C > 1$:

$$\tilde{\Phi}_f = 1 + 0.5(\tilde{\Phi}_C - 1) \quad \text{for } \tilde{\Phi}_C > 1 \quad (35)$$

and by second-order upwinding for negative $\tilde{\Phi}_C$:

$$\tilde{\Phi}_f = 1.5\tilde{\Phi}_C \quad \text{for } \tilde{\Phi}_C < 0 \quad (36)$$

but other functional relationships are possible. The dashed lines show extensions of equations (35) and (36) into the monotonic range, $0 < \tilde{\Phi}_C < 1$; note that they both pass through the 'second-order' point C, located at (0.5, 0.75). To avoid non-uniqueness near $\tilde{\Phi}_C \rightarrow 0_+$, the boundary OB

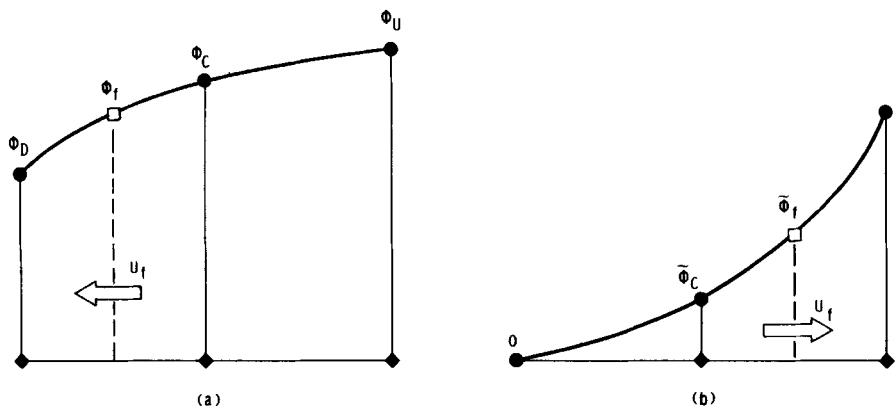


Figure 14. Definition of normalized variables according to equation (32): (a) original unnormalized variables; (b) corresponding diagram in terms of normalized variables

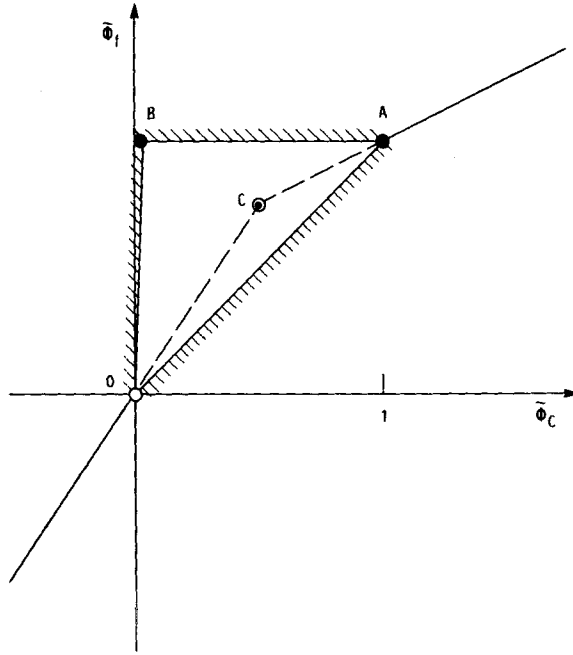


Figure 15. Universal limiter constraints in the Normalized Variable Diagram (NVD). Point C is located at (0.5, 0.75)

has a steep but finite positive slope. This introduces an additional constraint

$$\tilde{\Phi}_f \leq \text{const } \tilde{\Phi}_C \quad \text{near } \tilde{\Phi}_C \rightarrow 0_+ \quad (37)$$

where $\text{const} = O(100)$, for example.

At each stage of a pseudo-time-marching (Appendix II) or iterative solution, the universal limiter constraints are applied as follows:

- (i) For each CV face, note the direction of the (current) normal velocity component, thereby identifying Φ_U , Φ_C and Φ_D .
- (ii) Explicitly compute a tentative high-order multidimensional upwind-biased face-value, Φ_f .
- (iii) Compute the corresponding *normalized* face-value, $\tilde{\Phi}_f$, and the normalized adjacent upwind node-value, $\tilde{\Phi}_C$.
- (iv) If the point $(\tilde{\Phi}_C, \tilde{\Phi}_f)$ falls within the triangular region of Figure 15, simply proceed to the next CV face.
- (v) If not, $\tilde{\Phi}_f$ is limited to the nearest appropriate constraint boundary at the given $\tilde{\Phi}_C$ -value.
- (vi) The *unnormalized* face-value is then reconstructed by

$$\Phi_f = \tilde{\Phi}_f(\Phi_D - \Phi_U) + \Phi_U \quad (38)$$

- (vii) The same procedure is used for each CV face.

Then, in a time-marching algorithm, the (limited) convective fluxes and corresponding diffusive fluxes (computed using second-order central differencing) are now available for the explicit update step. Alternatively, iterative implicit solution can be implemented by introducing the downwind weighting factor, as now described.

The Downwind Weighting Factor

Instead of limiting the face variable directly, the *Downwind Weighting Factor* (DWF) is introduced as an auxiliary variable, thereby generating a compact implicit scheme suitable for tridiagonal solution methods. After explicitly computing the high-order multidimensional upwind-biased estimate, Φ_f , define

$$\text{DWF} = \frac{\Phi_f - \Phi_C}{\Phi_D - \Phi_C} \quad (39)$$

Since this is the same as

$$\text{DWF} = \frac{\tilde{\Phi}_f - \tilde{\Phi}_C}{1 - \tilde{\Phi}_C} \quad (40)$$

it is not difficult to see that, in terms of DWF, the universal limiter constraints, corresponding to Figure 15, become

$$0 \leq \text{DWF} \leq 1 \quad \text{for} \quad 0 < \tilde{\Phi}_C \leq 1 \quad (41)$$

or

$$\text{DWF} \leq \frac{(\text{const} - 1)\tilde{\Phi}_C}{(1 - \tilde{\Phi}_C)} \quad \text{near} \quad \tilde{\Phi}_C \rightarrow 0_+ \quad (42)$$

in the monotonic region, with, for example,

$$\text{DWF} = \frac{\tilde{\Phi}_C}{2(1 - \tilde{\Phi}_C)} \quad \text{for} \quad \tilde{\Phi}_C \leq 0 \quad (43)$$

and

$$\text{DWF} = 0.5 \quad \text{for} \quad \tilde{\Phi}_C > 1 \quad (44)$$

This is shown in Figure 16. Note that the point A, given by (1, 1) in Figure 15, has been stretched out into a vertical line in Figure 16. Point C is now at (0.5, 0.5).

Now rewrite the face-value (in terms of the known DWF) as

$$\Phi_f = \text{DWF} \Phi_U^{\text{TBC}} + (1 - \text{DWF}) \Phi_C^{\text{TBC}} \quad (45)$$

where 'TBC' stands for 'to-be-computed'—in the next iteration of an implicit line-sweep update. Note that the convective flux at each CV face now involves only the adjacent upwind and downwind 'TBC' node-values; but the DWF in equation (45) *implicitly* contains higher-order wide-stencil information (in addition to the universal limiter constraints). Clearly, when DWF's are computed for each CV face on a quadrilateral grid, the *implicit update stencil* consists of the central CV node-value itself, together with only the surrounding adjacent node-values—i.e. a compact $(2N + 1)$ -point stencil in N dimensions. This is the same compact stencil as used by a large number of 2D and 3D commercial and research codes of TEACH-like structure, based on tridiagonal line-sweep solution algorithms, thus immediately opening up the possibility of incorporating (in principle, arbitrarily) high-order non-oscillatory convection schemes into these well-established general-purpose elliptic solvers.

Using the popular compass-point notation,² the individual convected face-values are computed as follows. Considering the west face, for example, the face-value obtained from equation (45) will depend on the sign of the convecting velocity at the west face. If Φ_w^* is the initial higher-order estimate on the west face, the DWF is first computed according to

$$\text{DWF}_w^+ = \frac{\Phi_w^* - \Phi_w}{\Phi_C - \Phi_w} \quad \text{if} \quad u_w \geq 0 \quad (46)$$

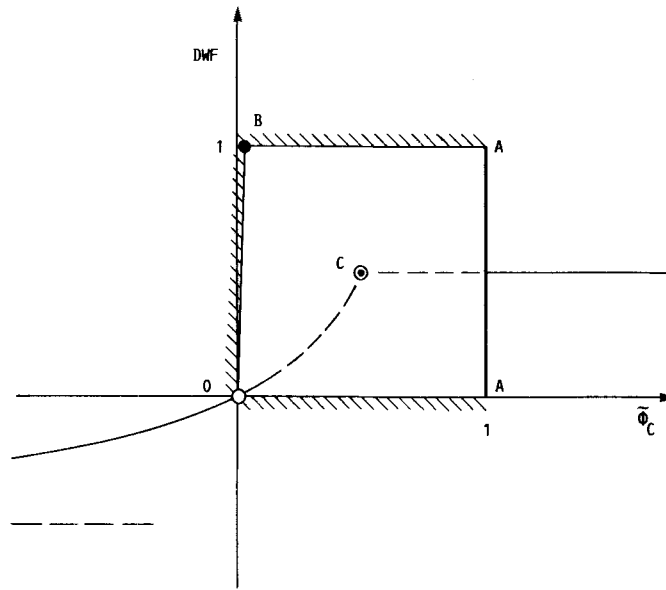


Figure 16. Universal limiter constraints (corresponding to Figure 15) in terms of the downwind weighting factor (DWF). Point C is at (0.5, 0.5). Note the singularity at $\Phi_C = 1$

or

$$DWF_w^- = \frac{\Phi_w^* - \Phi_C}{\Phi_w - \Phi_C} \quad \text{if } u_w < 0 \quad (47)$$

Then (the appropriate) DWF is limited according to Figure 16. The face-value used in the implicit update is then

$$\Phi_w = DWF_w^+ \Phi_P + (1 - DWF_w^+) \Phi_w \quad \text{for } u_w \geq 0 \quad (48)$$

or

$$\Phi_w = DWF_w^- \Phi_w + (1 - DWF_w^-) \Phi_P \quad \text{for } u_w < 0 \quad (49)$$

In either case, Φ_w is a linear combination of its two adjacent (upwind and downwind) node-values, with $\text{SGN}(u_w)$ as a parameter,

$$\Phi_w = \mathcal{L}_w^{DWF} [\Phi_w, \Phi_P; \text{SGN}(u_w)] \quad (50)$$

Similarly for the other faces of this particular CV cell. This results in an update (in three dimensions) of the form

$$a_P \Phi_P = a_W \Phi_w + a_S \Phi_S + a_B \Phi_B + a_E \Phi_E + a_N \Phi_N + a_T \Phi_T + b \quad (51)$$

which is, of course, identical to the form generated by first-order upwind or second-order central methods or combinations such as Hybrid, PLDS, or EDS.² Again, it should be stressed that the higher-order multidimensional information and the non-oscillatory universal limiter constraints are implicitly contained in the DWF's of each face rather than involving 'outlying' node-values that are then lumped into the explicit source term. The limiter constraints inherent in the DWF's guarantee non-oscillatory results, with stability and convergence properties similar to first-order methods ($DWF \equiv 0$)—but without introducing artificial numerical diffusion.

Non-oscillatory multidimensional results

Figure 17 shows results of applying the universal limiter constraints to the QUICK-2D scheme for the oblique-step test at $P_\Delta = 100$. These ULTRA-QUICK results should be compared to the unlimited QUICK results of Figure 11. Note that resolution remains sharp (reflecting the third-order accuracy) even though there are no overshoots or undershoots. Also note the concomitant reduction in error seen in Figure 17(d). But the great power of the universal limiter resides in the fact that it can be used with higher-order convection schemes. A dramatic increase in sharpness in the simulation of the near-discontinuity is seen in Figure 18, showing results for the same problem using ULTRA-5th upwinding for convection. As explained in Appendix III, this scheme uses (one-dimensional) fifth-order upwinding normal to each CV face, together with third-order (QUICK) transverse-curvature terms; second-order-central terms are adequate for diffusion. As θ is varied from 0° to 90° , the total error is never more than about 5.2. Considering the fact that the error is a cumulative value summed over 625 grid-points, these ULTRA-5th results are seen to be highly accurate.

Cost-effectiveness and adaptive stencil expansion

Now that it has been established that viable non-oscillatory higher-order methods can be easily devised, a natural question to ask is: which is more cost-effective in terms of overall computer usage (*for a prescribed accuracy*), a fine-grid computation using a low-order method, or a coarse-grid calculation using a higher-order scheme? Gaskell and Lau²⁷ compared first-order upwinding with the third-order QUICK scheme and a non-oscillatory version (similar to ULTRA-QUICK),

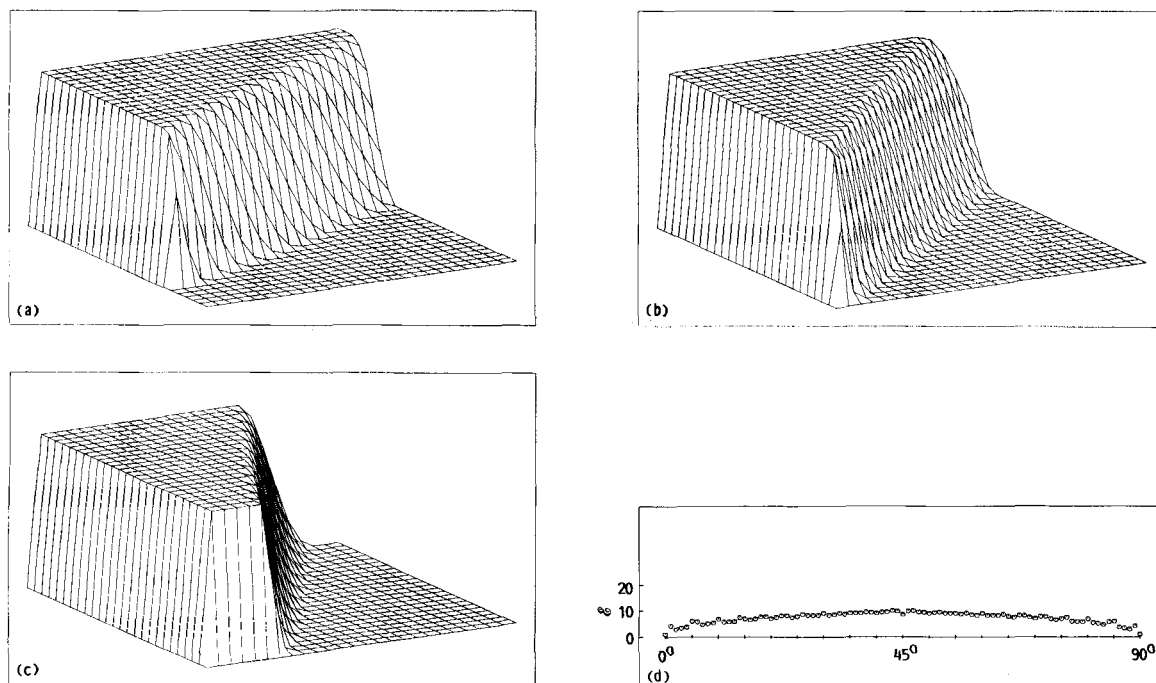


Figure 17. ULTRA-QUICK oblique-step results for $P_\Delta = 100$: (a) $\theta = 30^\circ$, $\epsilon = 9.2$; (b) $\theta = 45^\circ$, $\epsilon = 8.6$; (c) $\theta = 60^\circ$, $\epsilon = 9.2$; (d) ϵ as a function of θ (maximum = 10.2 at 43° or 47°)

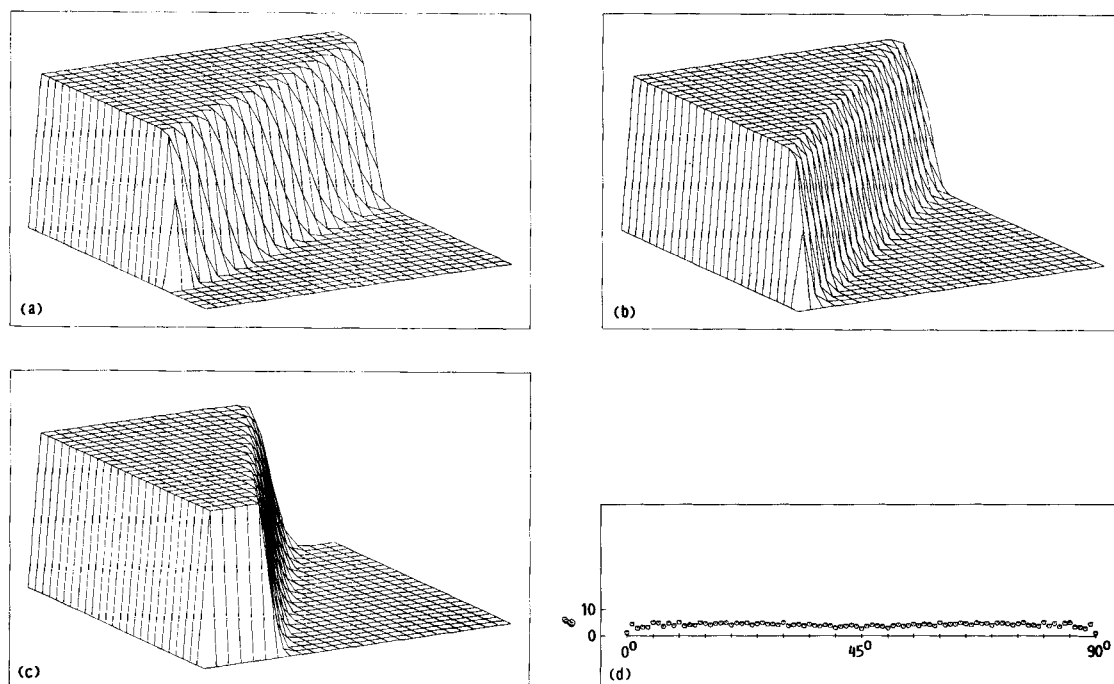


Figure 18. ULTRA-5th-upwind oblique-step results for $P_A = 100$: (a) $\theta = 30^\circ$, $\mathcal{E} = 5.0$; (b) $\theta = 45^\circ$, $\mathcal{E} = 2.8$; (c) $\theta = 60^\circ$, $\mathcal{E} = 5.0$; (d) \mathcal{E} as a function of θ (maximum = 5.2 at 10° or 80°)

using successive grid refinement on the two-dimensional oblique-step test. For a prescribed accuracy, first-order methods required such a fine grid, compared with the practical grid third-order methods, that CPU time was larger by three orders of magnitude! This disparity would be even more impressive in three dimensions. Another obvious question is: what order is 'optimal' in the above sense of cost-effectiveness? Clearly second-order upwinding (which involves the same stencil as QUICK or ULTRA-QUICK) is not. Higher-order non-oscillatory methods such as ULTRA-5th require more operations (than ULTRA-QUICK) at each grid-point; but perhaps this can be offset by the greater accuracy available on a coarser grid.

Figure 19 gives some indication of optimality in the two-dimensional case. Part (a) of the figure shows global absolute error versus number of grid-points for several different methods applied to the infinite- P_A oblique-step test for $\theta = 45^\circ$. Part (b) shows the corresponding CPU time (without cost-adjustment for storage). The results, corresponding to a prescribed accuracy from part (a), are cross-plotted in part (c) of the figure. Even on a logarithmic scale, the 'cost' of the first-order method is off-scale. As expected, third-order methods are significantly better than second-order upwinding (because of better accuracy for essentially the same cost-per-grid-point); but fifth and higher-order methods are somewhat less cost-effective than third. On the other hand, for a given grid-size, Figure 18 shows that ULTRA-5th, in particular, can give dramatically sharper resolution of discontinuities than the corresponding third-order scheme. This suggests a simple strategy of *adaptive stencil expansion* that is proving to be extremely cost-effective in both steady-state and time-accurate transient simulations.³⁹

Use third-order ULTRA-QUICK in 'smooth' regions of the flow; then on the basis of some 'non-smoothness' monitor, switch to a higher-order (ULTRA) scheme *locally*, as needed.

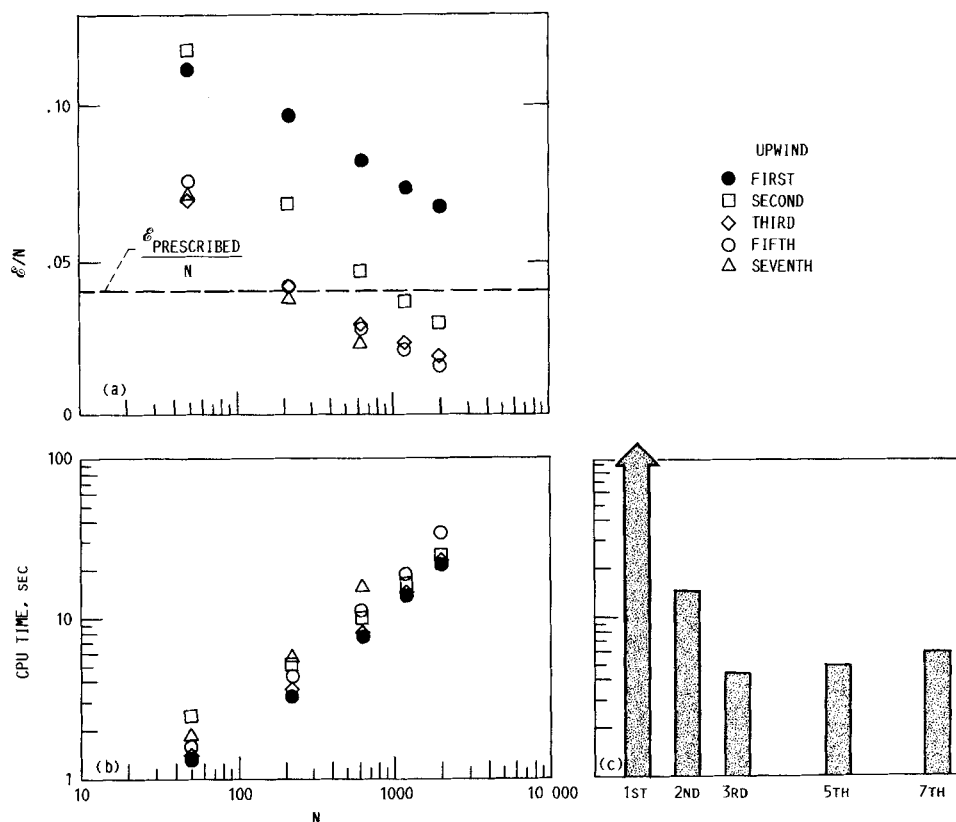


Figure 19. Cost-effectiveness of higher-order schemes: (a) error as a function of grid refinement; (b) CPU time as a function of grid refinement; (c) CPU time for various schemes corresponding to the *prescribed* error shown in part (a)

Since 'smooth' regions correspond to small values of the convected variables' change in gradient (i.e. curvature), a suitable monitor at face $(i + \frac{1}{2})$, for example, would be the absolute average 'curvature' (normal to the CV face):

$$\text{CURVAV} = 0.5 |(\Phi_{i+2} - \Phi_{i+1}) - (\Phi_i - \Phi_{i-1})| \quad (52)$$

This, of course, is also a good indicator of sudden changes in gradient near discontinuities. Thus, if CURVAV is below a prescribed threshold, the algorithm uses the optimally cost-effective ULTRA-QUICK scheme. Even when discontinuities are present, this will account for the bulk of the flow domain—since, by definition, discontinuities (when tightly resolved) involve only a very few number of grid-points in narrow isolated regions. Wherever CURVAV exceeds the threshold, the algorithm automatically expands to a wider stencil, such as ULTRA-5th, and uses this more accurate scheme in the appropriate *local* regions. In most cases of practical interest, the additional 'cost' is imperceptible compared with a global ULTRA-QUICK calculation; however, resolution of near-discontinuities is dramatically enhanced. Additional thresholds can be used for further adaptive stencil expansion to invoke (in principle, arbitrarily) higher-order resolution, if desired. In addition, it is desirable to use a higher-order (ULTRA) scheme where the local absolute normal 'gradient'

$$\text{GRAD} = |\Phi_{i+1} - \Phi_i| \quad (53)$$

across the CV face exceeds a given threshold. This strategy has been used up to ninth order in inviscid transient calculations³⁹ in order to resolve extremely narrow pulses in the convected variable. For steady-state calculations, it appears that an adaptive ULTRA-QUICK/5th/7th-order convection scheme has a number of attractive attributes, including cost-effectiveness (high coarse-grid accuracy), reliability (excellent stability and convergence properties) and ease of coding. The order-switching strategy is shown schematically in Figure 20. Results of the oblique-step test (at $P_\Delta = 100$, with second-order diffusion terms) are seen in Figure 21 to be essentially exact for all practical purposes. Even higher-order adaptive stencil expansion could be developed for specialty applications.

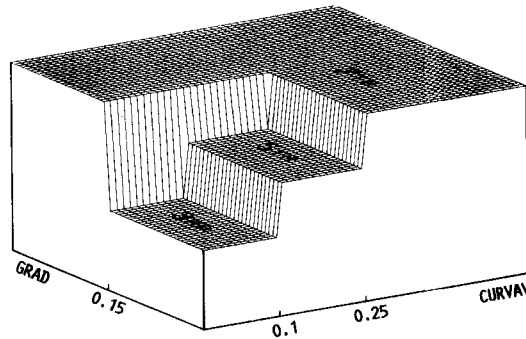


Figure 20. Schematic diagram of order-switching strategy used in the locally adaptive stencil expansion algorithm

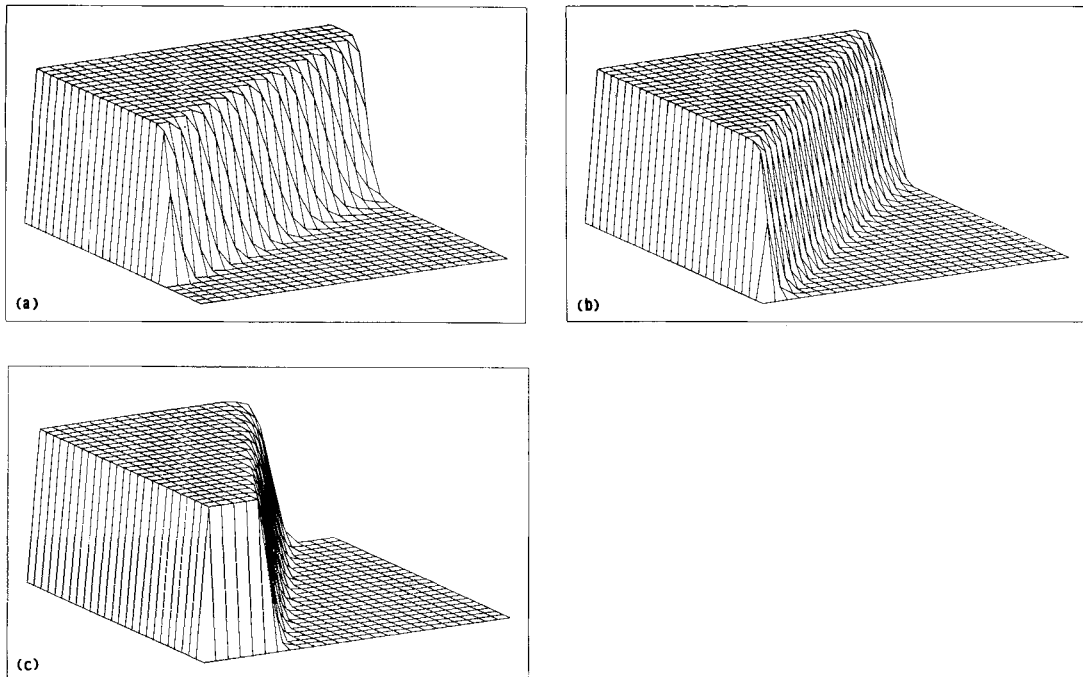


Figure 21. ULTRA-3rd/5th/7th-upwind oblique-step results for $P_\Delta = 100$: (a) $\theta = 30^\circ$, $\mathcal{E} = 4/3$; (b) $\theta = 45^\circ$, $\mathcal{E} = 2/2$; (c) $\theta = 60^\circ$, $\mathcal{E} = 4/3$

Variable-curvature factor

For second- and third-order methods, the normalized convected CV face-value, $\tilde{\Phi}_f$, is a single-valued function of $\tilde{\Phi}_C$, and the curve representing this relationship in the NVD passes through the point C of Figure 15. Passing through C guarantees second-order accuracy; third-order accuracy (in a control-volume formulation) requires a slope of 3/4 at C (see Appendix I). In terms of unnormalized variables, such schemes can always be written

$$\Phi_f = 0.5(\Phi_D + \Phi_C) - \text{VCF}(\Phi_D - 2\Phi_C + \Phi_U) \quad (54)$$

where $\text{VCF} = \text{VCF}(\tilde{\Phi}_C)$ is the variable-curvature factor. For third-order methods, transverse-curvature terms¹³ should be added for consistency. Equation (54) can be written in terms of normalized variables, as follows:

$$\tilde{\Phi}_f = 0.5(1 + \tilde{\Phi}_C) - \text{VCF}(1 - 2\tilde{\Phi}_C) \quad (55)$$

Rearranging gives

$$\text{VCF} = \frac{(1 + \tilde{\Phi}_C - 2\tilde{\Phi}_f)}{2(1 - 2\tilde{\Phi}_C)} = \text{VCF}(\tilde{\Phi}_C) \quad (56)$$

when $\tilde{\Phi}_f(\tilde{\Phi}_C)$ is known. Note that this expression is determinate at $\tilde{\Phi}_C = 0.5$ for curves passing through point C. It is thus a simple matter to convert the universal limiter constraints of Figure 15 into constraints on VCF; these are shown in Figure 22. For reference, the figure also shows the third-order QUICK value, $\text{VCF} \equiv 1/8$. ULTRA-QUICK is shown by the heavy solid lines. Second-order central differencing corresponds to $\text{VCF} \equiv 0$; whereas second-order upwinding has $\text{VCF} \equiv 1/2$. Third-order accuracy for a given 'non-linear' scheme requires $\text{VCF} = 1/8$ at $\tilde{\Phi}_C = 1/2$.

In an iterative procedure, VCF is computed from equation (56) based on current values (of $\tilde{\Phi}_C$). Then equation (54) is written in terms of 'to-be-computed' values

$$\Phi_f = 0.5(\Phi_D^{\text{TBC}} + \Phi_C^{\text{TBC}}) - \text{VCF}(\Phi_D^{\text{TBC}} - 2\Phi_C^{\text{TBC}} + \Phi_U^{\text{TBC}}) \quad (57)$$

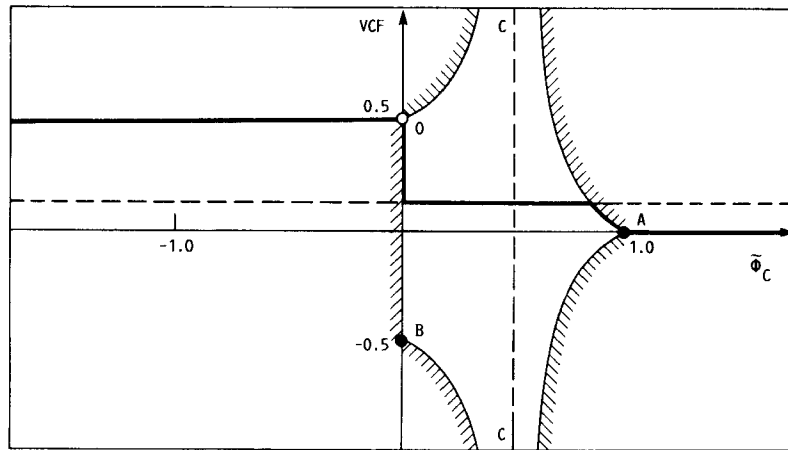


Figure 22. Universal limiter boundaries portrayed in terms of the variable curvature factor. Note the singularity at $\tilde{\Phi}_C = 0.5$. The straight lines through O and A correspond to those in Figure 15. The dashed line shows the QUICK value: $\text{VCF} \equiv 1/8$

implying a pentadiagonal matrix algorithm (PDMA) for line-sweep solution. This technique was originally developed by Gaskell and Lau²⁷ using a curvature correction, α , from the default value of $1/8$; i.e., in terms of the present notation,

$$\alpha(\tilde{\Phi}_C) = \text{VCF}(\tilde{\Phi}_C) - 1/8 \quad (58)$$

Figure 23 shows another third-order scheme based on an exponential upwinding or linear extrapolation refinement of third-order upwinding known as EULER.²⁸ Note the alternative treatment in the non-monotonic regions.

For reference, a pentadiagonal compass-point algorithm proceeds as follows:

- (i) For each CV face, compute VCF^+ or VCF^- , depending on $\text{SGN}(u_f)$.
- (ii) The VCF value may be under-relaxed to enhance convergence.²⁷
- (iii) Then for a typical, say west, face

$$\Phi_w = (0.5 - \text{VCF}_w^+) \Phi_P + (0.5 + 2\text{VCF}_w^+) \Phi_W - \text{VCF}_w^+ \Phi_{WW} \quad \text{for } u_w \geq 0 \quad (59)$$

or

$$\Phi_w = (0.5 - \text{VCF}_w^-) \Phi_W + (0.5 + 2\text{VCF}_w^-) \Phi_P - \text{VCF}_w^- \Phi_E \quad \text{for } u_w < 0 \quad (60)$$

In either case, Φ_w is a linear combination of four adjacent node-values in a direction normal to the face (two upwind and two downwind), with $\text{SGN}(u_w)$ as a parameter:

$$\Phi_w = \mathcal{L}_w^{\text{VCF}} [\Phi_{WW}, \Phi_W, \Phi_P, \Phi_E; \text{SGN}(u_w)] \quad (61)$$

(Inclusion of transverse curvature introduces additional terms which can be handled explicitly.) Similarly for the other faces of this CV cell. This results in an overall three-dimensional update algorithm of the form

$$\begin{aligned} a_P \Phi_P &= a_{WW} \Phi_{WW} + a_{SS} \Phi_{SS} + a_{BB} \Phi_{BB} + a_{EE} \Phi_{EE} + a_{NN} \Phi_{NN} + a_{TT} \Phi_{TT} \\ &+ a_W \Phi_W + a_S \Phi_S + a_B \Phi_B + a_E \Phi_E + a_N \Phi_N + a_T \Phi_T + b \end{aligned} \quad (62)$$

which is solved most effectively by alternating-direction *pentadiagonal* line-sweep iteration.²⁷ Tridiagonal methods could, of course, be used, taking care to place outlying—and certain other¹⁷—terms in the explicit source term; this, however, is not recommended as it appears to be somewhat less felicitous than the straight-forward (and highly efficient) PDMA technique.

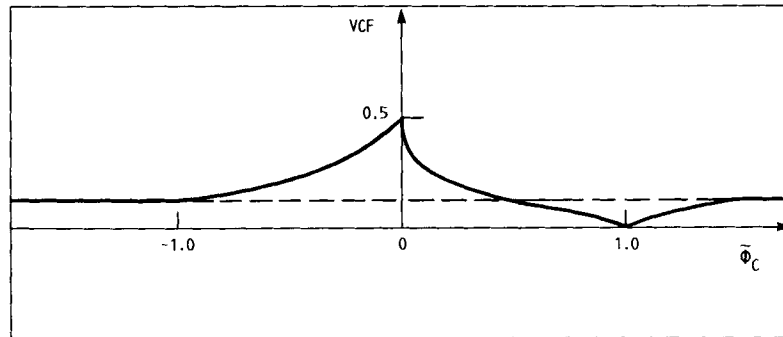


Figure 23. Variable curvature factor for the EULER-QUICK scheme. Third-order accuracy requires $\text{VCF} = 1/8$ at $\tilde{\Phi}_C = 1/2$. Note the alternate treatment in the non-monotonic regions ($\tilde{\Phi}_C < 0$ and $\tilde{\Phi}_C > 1$)

Relationship to TVD schemes

All of the so-called 'shock-capturing' and 'total-variation-diminishing' (TVD) schemes currently used in many gasdynamic codes²⁴ can be immediately adapted to incompressible convective modelling. Since these methods use the same stencil as QUICK (without transverse curvature), they can be described within the framework of the variable-curvature-factor technique. They can also, of course, be represented as specific curves in the downwind-weighting-factor diagram or the normalized-variable diagram. For example, Figures 24 and 25 show three well-known schemes of this type in terms of the NVD and the DWF, respectively: Superbee (a supercompressive scheme), Minmod (a relatively diffusive scheme)²⁶ and the 'harmonic' scheme devised by van Leer.⁴⁰

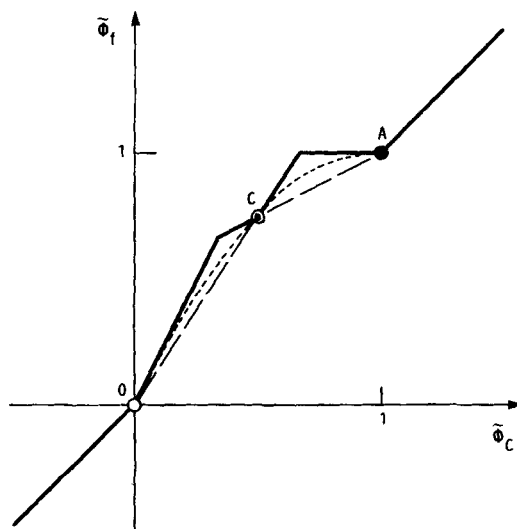


Figure 24. Normalized-variable diagram for Superbee (heavy piecewise linear graph), the harmonic scheme (dotted parabolic curve) and Minmod (dashed lines). All schemes follow $\tilde{\Phi}_f = \tilde{\Phi}_c$ in the non-monotonic regions

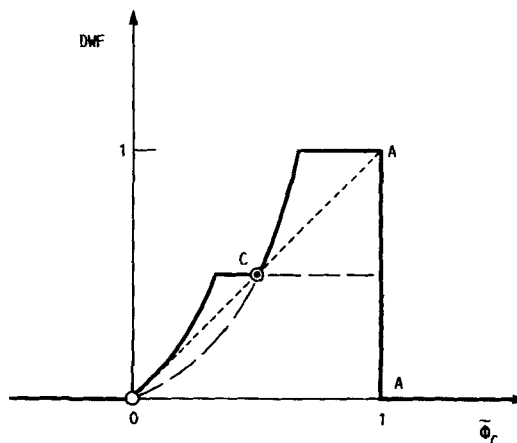


Figure 25. Downwind weighting factor variation for the Superbee, harmonic and Minmod schemes. Same legend as in Figure 24

All shock-capturing and TVD schemes in common use conform to an overly restrictive limiter²⁵ which tends to make them more diffusive than necessary. In terms of normalized variables, this restriction is

$$\tilde{\Phi}_f \leq 2\tilde{\Phi}_c \quad \text{for} \quad 0 \leq \tilde{\Phi}_c \leq 0.5 \quad (63)$$

Superbee, for example, can be described as a hybrid between second-order central and second-order upwinding, constrained by inequality (63)—and by $\tilde{\Phi}_f \leq 1$ in the remainder of the monotonic region. Figure 26 shows the NVD for a scheme similar in philosophy to Superbee but constrained only by the universal limiter; this might appropriately be called ULTRA-B. In fact, the basic idea of just such a method was originally proposed by Roe for gasdynamic methods⁴¹ and, coincidentally, named 'Ultrabee'. Figure 27 shows the 45° oblique-step test at $P_\Delta = 100$ using Minmod, the harmonic scheme and ULTRA-B (or Ultrabee). Note the diffusive nature of Minmod; the harmonic scheme gives results similar to those of ULTRA-QUICK; by contrast, the supercompressive ULTRA-B scheme gives extremely sharp monotonic resolution—in fact, slightly *sharper than the exact solution* at this finite grid Peclet number.

Although the step-resolution properties of simple supercompressive schemes such as ULTRA-B are very impressive, it should be realized that the sharp resolution is actually obtained by the local introduction of *negative* numerical diffusion, which is directly responsible for artificial steepening of discontinuities. Unfortunately, such methods have a tendency to artificially steepen *all* profiles—with concomitant flattening of peaks (due to mass conservation). This drawback is seen in Figure 28, which shows oblique convection without diffusion (at $\theta = 45^\circ$) of a semi-elliptical upstream boundary profile simulated using ULTRA-B; the (infinite- P_Δ) exact solution is shown for reference. By contrast, Figure 29(a) shows the same test simulated by ULTRA-QUICK/3rd/5th/7th. Note that, in this case, the sudden change in gradient at the base of the profile is well captured without the extreme clipping produced by the supercompressive scheme. However, there is still some loss of resolution near the local maximum because of the action of the

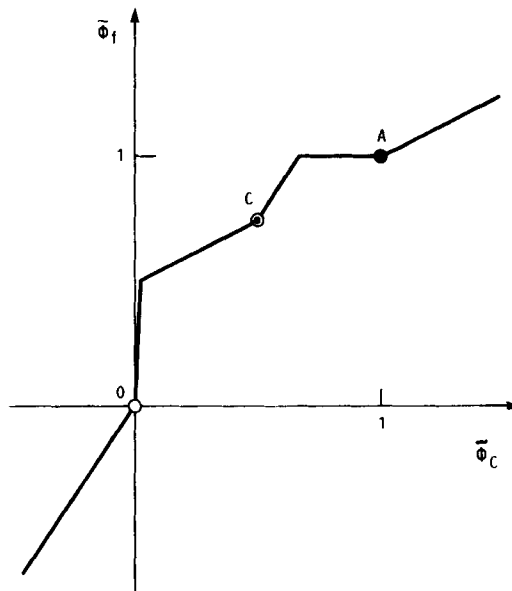


Figure 26. Normalized variable diagram for the ULTRA-B scheme. Compare with Superbee in Figure 24. Note the significant difference near $\tilde{\Phi}_c \rightarrow 0_+$

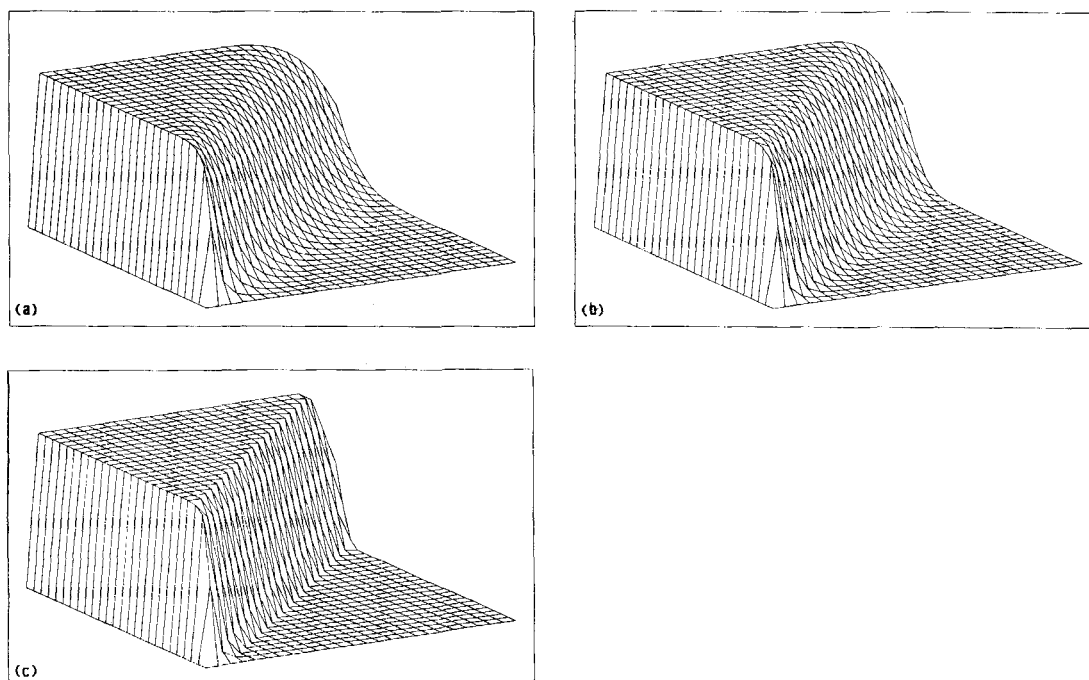


Figure 27. Oblique-step results for $\theta = 45^\circ$ and $P_\Delta = 100$ using: (a) Minmod, $\varepsilon = 26.4$; (b) the harmonic scheme, $\varepsilon = 17.1$; (c) ULTRA-B, $\varepsilon = 4.0$

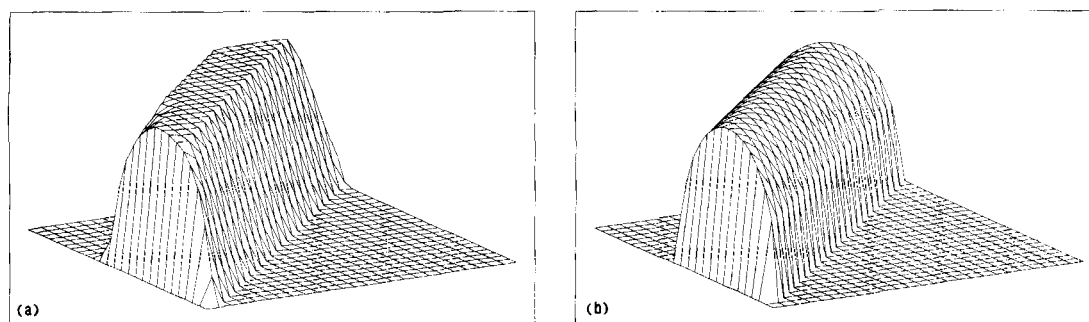


Figure 28. Oblique convection (at $\theta = 45^\circ$, $P_\Delta = \infty$) of an elliptic profile imposed at the inflow boundary: (a) ULTRA-B solution showing artificial steepening and concomitant clipping, $\varepsilon = 17.2$; (b) exact solution for reference

universal limiter. This problem, in turn, can be largely resolved by switching off the limiter in regions of true local extrema, as seen in Figure 29(b). The problem then becomes one of pattern-recognition: near physical local extrema, the limiter needs to be switched off; but it should remain active near discontinuous jumps or sudden changes in gradient to suppress spurious unphysical overshoots or undershoots. An automatic discriminator of this type has been constructed for *one-dimensional* steady-state⁷ and transient³⁹ cases. In Figure 29(b), the limiter is simply artificially switched off for $\Phi \geq 0.5$. Clearly, this strategy cannot be used in general. An automatic discriminator for *multidimensional* steady-state flow is currently under development.

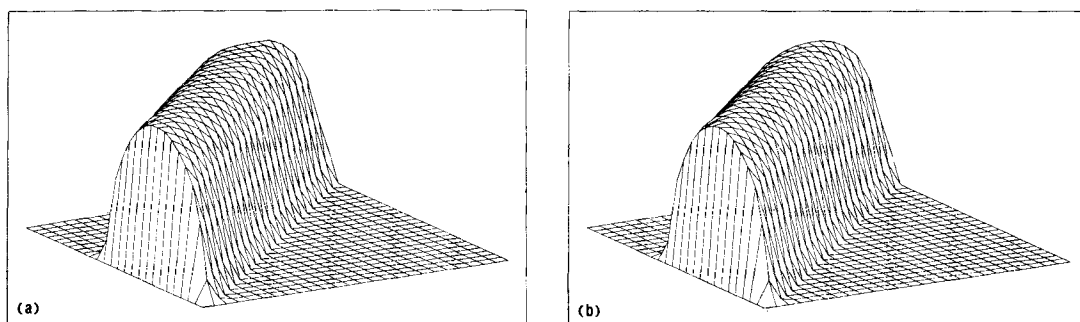


Figure 29. Oblique convection of the elliptic profile using (a) ULTRA-3rd/5th/7th, $\mathcal{E} = 10^{-7}$; (b) ULTRA-3rd/5th/7th with limiter-relaxation near local maxima, $\mathcal{E} = 10^{-1}$

Rotating velocity field

To get some idea of the effect of spatially varying velocity, pure convection (without diffusion) of boundary-specified profiles in a velocity field given by solid-body rotation represents an effective benchmark problem. In a two-dimensional conservative, finite-volume, formulation, it is convenient to have the stream-function values available at control-volume corners; then the CV face-average convecting velocity is simply the difference of the corner stream-function values across the face. The stream-function used in the proposed benchmark test is

$$\psi(x, y) = \frac{\omega_0}{2} [(x - x_c)^2 + (y - y_c)^2] \quad (64)$$

where ω_0 is a specified angular velocity and (x_c, y_c) is the location of the rotation axis. The velocity field is shown schematically in Figure 30.

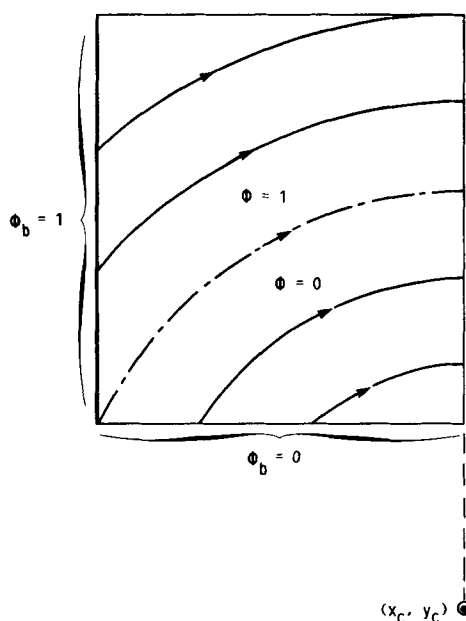


Figure 30. Schematic diagram of the rotating velocity field boundary-step problem

Figure 31 gives the exact solution for a sharp non-diffusing ($P_\Delta = \infty$) complementary-error-function step in boundary value at the lower left corner. Figure 32 shows results for first-order upwinding (\equiv Hybrid \equiv PLDS \equiv EDS in this infinite- P_Δ case). Figures 33 to 35 show unlimited forms of second-, third- and fifth-order upwinding. Figures 36 and 37 give Minmod and ULTRA-B results. Finally, Figure 38 shows ULTRA-QUICK/5th/7th results. These results and the corresponding global errors listed in the captions are self-explanatory.

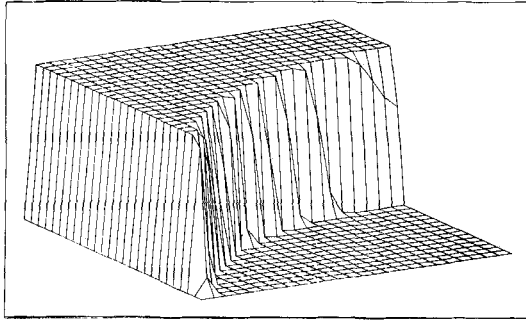


Figure 31. Exact solution of the rotating velocity problem for $P_\Delta = \infty$ and a narrow complementary-error-function profile jump at the upstream boundary corner

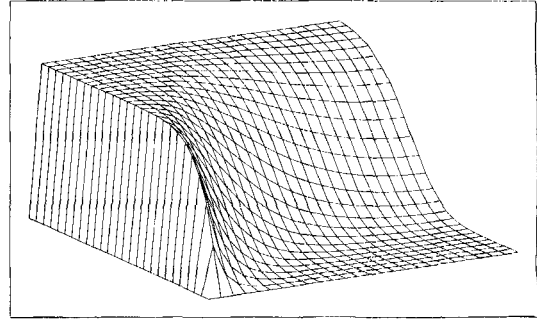


Figure 32. First-order upwind (\equiv Hybrid \equiv PLDS \equiv EDS) results for the rotating step problem; $\mathcal{E} = 65.3$

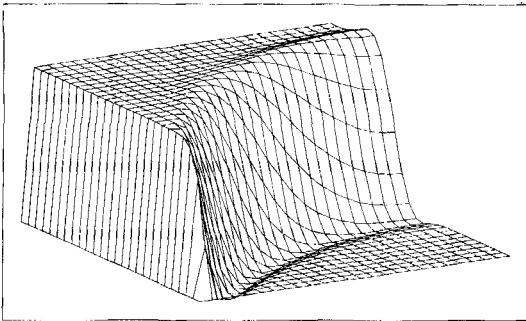


Figure 33. Second-order upwind results for the rotating step problem; $\mathcal{E} = 27.3$

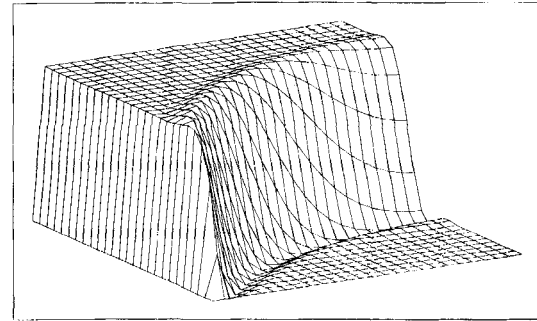


Figure 34. Unlimited QUICK-2D results for the rotating step problem; $\mathcal{E} = 18.9$

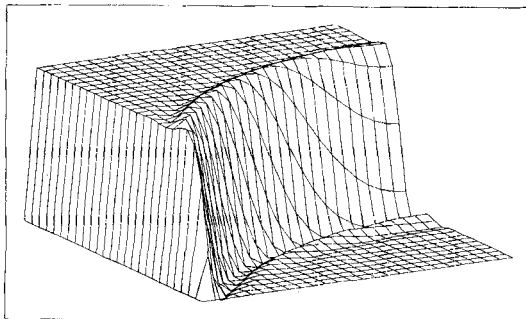


Figure 35. Unlimited fifth-order upwind results for the rotating step problem; $\mathcal{E} = 16.1$

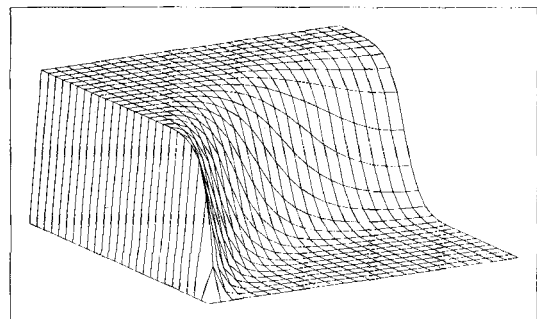


Figure 36. Minmod results for the rotating step problem; $\mathcal{E} = 30.6$

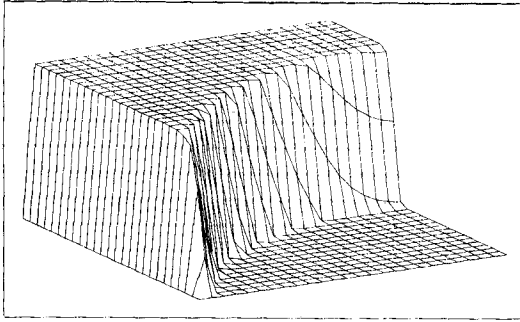


Figure 37. ULTRA-B results for the rotating step problem; $\mathcal{E} = 7.7$

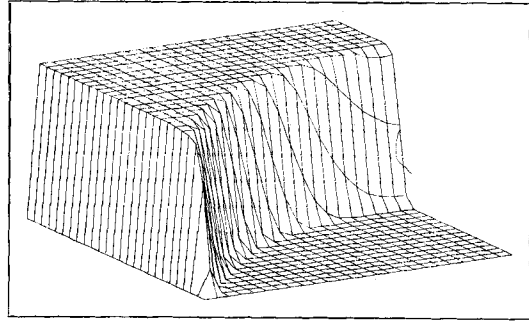


Figure 38. ULTRA-3rd/5th/7th results for the rotating step problem; $\mathcal{E} = 9.1$

CONCLUSION

In terms of normalized variables, first-order upwinding is represented by

$$\tilde{\Phi}_f = \tilde{\Phi}_c \quad (65)$$

which, in the NVD, is a straight line passing through (0, 0) and (1, 1). It thus conforms (marginally) to the universal limiter constraints (Figure 15) and, thereby, produces non-oscillatory results. As shown by Godunov,⁴² it is the only 'linear' scheme (i.e. in the present terminology, $\tilde{\Phi}_f$ is a linear function of $\tilde{\Phi}_c$) which possesses this property, as can easily be seen from Figure 15. TVD schemes are based on single-valued *non-linear* relationships between $\tilde{\Phi}_f$ and $\tilde{\Phi}_c$ but also require the corresponding NVD curves to pass through (0, 0) and (1, 1), with certain other (in some respects, unnecessary) restrictions. If the NVD curve passes through (0.5, 0.75), the scheme is second-order accurate (or third-order if it passes through this point with a slope of 3/4); if not, the scheme is only first-order accurate. Schemes with generally larger values of $\tilde{\Phi}_f$ (at a given $\tilde{\Phi}_c$ value) tend to be more 'compressive' than schemes with lower values. Thus, Superbee is more compressive than ULTRA-QUICK, for example, whereas Minmod is more diffusive. First-order upwinding, of course, is seen to be the most diffusive of all non-oscillatory schemes.

Higher-order schemes cannot be represented by a single curve in the $(\tilde{\Phi}_c, \tilde{\Phi}_f)$ plane; however, they can still be constrained to pass through (0, 0) and (1, 1), which appears to be a basic condition for non-oscillatory results. In the monotonic range ($0 \leq \tilde{\Phi}_c \leq 1$), the downwind constraint, $\tilde{\Phi}_f \leq 1$, guarantees uniqueness, whereas the upwind constraint, $\tilde{\Phi}_f \geq \tilde{\Phi}_c$, eliminates stair-casing. The additional *ad hoc* constraint, $\tilde{\Phi}_f \leq \text{const} \tilde{\Phi}_c$, avoids non-uniqueness near $\tilde{\Phi}_c \rightarrow 0_+$. The resulting triangular region in the NVD, Figure 15, constitutes the steady-flow universal limiter in the monotonic range. In the non-monotonic regime, there is considerable flexibility, provided the constraints are consistent with passing through (0, 0) and (1, 1), and that $\partial \tilde{\Phi}_f / \partial \tilde{\Phi}_c$ remains positive and finite (for uniqueness). It is not necessary to specify a single-valued function in this regime; this is usually done purely as a matter of convenience.

As has been shown, it is a simple matter to design higher-order non-oscillatory convection schemes and to frame them in terms of simple explicit time-marching techniques or (by using the downwind weighting factor) traditional TDMA iterative algorithms. The special class of second- and third-order schemes (including all currently used TVD schemes) can also be constructed using straightforward PDMA iterative methods, using the variable-curvature-factor technique—essentially equivalent to Gaskell-and-Lau's 'curvature compensation' method. Existing codes based on a TEACH-like structure involving iterative line-sweep TDMA solvers can now be

immediately upgraded to incorporate cost-effective higher-order non-oscillatory methods such as ULTRA-QUICK/5th/7th. Alternatively, because of efficiencies involved in vectorization and parallel processing, the simple explicit time-marching algorithm may be more attractive. In any case, there is certainly no longer any reason why grossly artificially diffusive methods, such as Hybrid, PLDS (or EDS), should be used under any circumstances. The availability of ULTRA-SHARP schemes, giving non-oscillatory high-accuracy results on coarse grids, means that computational fluid dynamicists will at last be able to focus their attention on physical modelling of complex fluid phenomena and on reliable practical three-dimensional simulations for analysis and design, without being plagued by spurious oscillations or non-convergence or by the (less obvious but potentially more dangerous) debilitating inaccuracies attributable to massive artificial diffusion.

ACKNOWLEDGEMENTS

Portions of this work were supported by the National Science Foundation under contract ECS-8904595 and part of the first author's research was carried out at the Institute for Computational Mechanics in Propulsion (ICOMP) at the NASA Lewis Research Center (work funded under Space Act Agreement C99066G).

APPENDIX I

Formal accuracy of the QUICK scheme

There has been some confusion in the literature⁴³ regarding the formal order of accuracy of the QUICK scheme in terms of truncation error. The problem seems to have arisen through a confusion of the point-simulation of the convective derivative with the corresponding control-volume formulation. It is enough to consider the simplest case of one-dimensional constant-velocity flow using a uniform grid. At third (and higher) order, there is a difference between

$$\left(\frac{\partial \Phi}{\partial x} \right)_i \quad (A1)$$

on the one hand, and the integrated control-volume (CV) conservative expression

$$\frac{\Phi_r - \Phi_l}{\Delta x} \quad (A2)$$

where the subscripts refer to the right and left CV face-values of the convected variable. A Taylor-series expansion of (A1) results in³⁰

$$\left(\frac{\partial \Phi}{\partial x} \right)_i = \frac{\Phi_{i+1} - \Phi_{i-1}}{2\Delta x} - \frac{\Phi_{i+1} - 3\Phi_i + 3\Phi_{i-1} - \Phi_{i-2}}{6\Delta x} + O(\Delta x^3) \quad (A3)$$

where an upwind bias is used on the third difference, assuming a positive convecting velocity. This could be split into two terms, resulting in a conservative CV form

$$\left(\frac{\partial \Phi}{\partial x} \right)_i = \frac{\Phi_r^* - \Phi_l^*}{\Delta x} + O(\Delta x^3) \quad (A4)$$

where

$$\Phi_r^* = \frac{1}{2}(\Phi_{i+1} + \Phi_i) - \frac{1}{6}(\Phi_{i+1} - 2\Phi_i + \Phi_{i-1}) \quad (A5)$$

and Φ_l^* is obtained from Φ_r^* by decreasing all indexes by 1.

However, equation (A4) does *not* represent the control-volume expression given by (A2) to third order. To see this, make Taylor expansions of the node-values about the CV *face* locations. For example,

$$\Phi_{i+1} = \Phi_r + \Phi'_r \left(\frac{\Delta x}{2} \right) + \frac{1}{2} \Phi''_r \left(\frac{\Delta x}{2} \right)^2 + \frac{1}{6} \Phi'''_r \left(\frac{\Delta x}{2} \right)^3 + \frac{1}{24} \Phi^{(iv)}_r \left(\frac{\Delta x}{2} \right)^4 + \dots \quad (\text{A6})$$

$$\Phi_i = \Phi_r - \Phi'_r \left(\frac{\Delta x}{2} \right) + \frac{1}{2} \Phi''_r \left(\frac{\Delta x}{2} \right)^2 - \frac{1}{6} \Phi'''_r \left(\frac{\Delta x}{2} \right)^3 + \frac{1}{24} \Phi^{(iv)}_r \left(\frac{\Delta x}{2} \right)^4 - \dots \quad (\text{A7})$$

$$\Phi_{i-1} = \Phi_r - \Phi'_r \left(\frac{3\Delta x}{2} \right) + \frac{1}{2} \Phi''_r \left(\frac{3\Delta x}{2} \right)^2 - \frac{1}{6} \Phi'''_r \left(\frac{3\Delta x}{2} \right)^3 + \frac{1}{24} \Phi^{(iv)}_r \left(\frac{3\Delta x}{2} \right)^4 - \dots \quad (\text{A8})$$

So that linear interpolation across the right face would give

$$\Phi_r^L = \frac{1}{2}(\Phi_{i+1} + \Phi_i) = \Phi_r + \Phi'_r \left(\frac{\Delta x^2}{8} \right) + O(\Delta x^4) \quad (\text{A9})$$

It is easily seen that the 1/6 factor in equation (A5) does not completely cancel the Φ'_r term. In order to cancel this term completely, one needs the QUICK formulation

$$\Phi_r^Q = \frac{1}{2}(\Phi_{i+1} + \Phi_i) - \frac{1}{8}(\Phi_{i+1} - 2\Phi_i + \Phi_{i-1}) \quad (\text{A10})$$

i.e.

$$\Phi_r^Q = \Phi_r + \frac{1}{16} \Phi'''_r \Delta x^3 + \dots \quad (\text{A11})$$

Thus, for the complete CV term,

$$\frac{\Phi_r^Q - \Phi_\ell^Q}{\Delta x} = \frac{\Phi_r - \Phi_\ell}{\Delta x} + \frac{1}{16} \left[\frac{(\Phi'''_r - \Phi'''_\ell)}{\Delta x} \right] \Delta x^3 + \dots \quad (\text{A12})$$

and, of course, in the limit $\Delta x \rightarrow 0$, the term in square brackets becomes $\Phi^{(iv)}$, so that

$$\frac{\Phi_r^Q - \Phi_\ell^Q}{\Delta x} = \frac{\Phi_r - \Phi_\ell}{\Delta x} + O(\Delta x^3) \quad (\text{A13})$$

Since a conservative flux-based formulation should be consistent with the CV form, the QUICK simulation is the appropriate one to use. Note that several other discretization schemes can be represented in terms of a ‘curvature factor’

$$\Phi_r^D = \frac{1}{2}(\Phi_{i+1} + \Phi_i) - CF(\Phi_{i+1} - 2\Phi_i + \Phi_{i-1}) \quad (\text{A14})$$

(with an analogous expression for negative convecting velocities). For example, second-order upwinding has $CF = 1/2$, and Fromm’s method⁴⁴ has $CF = 1/4$ (and, of course, central differencing is equivalent to $CF = 0$). The distinction between equations (A5) and (A10) thus hinges on the factors 1/6 and 1/8, respectively. For a steady-state control-volume formulation, the 1/8-factor gives the appropriate third-order accuracy. Interestingly enough, for the corresponding time-accurate control-volume formulation of *unsteady* convection-dominated flows, an additional factor of 1/24 (together with a Courant-number-dependent term) must be added to the 1/8-factor, thereby reconstructing the value of 1/6. This was explained—but evidently not universally understood—over ten years ago, when the QUICK and QUICKEST algorithms were initially published.³⁷

In terms of normalized variables, equation (A10) becomes

$$\tilde{\Phi}_r^Q = 0.5(1 - \tilde{\Phi}_C) - 0.125(1 - 2\tilde{\Phi}_C) \quad (\text{A15})$$

or, more simply

$$\tilde{\Phi}_r^Q = 0.75 + 0.75(\tilde{\Phi}_C - 0.5) \quad (\text{A16})$$

Similarly, equation (A14) becomes

$$\tilde{\Phi}_r^D = 0.75 + (2CF + 0.5)(\tilde{\Phi}_C - 0.5) \quad (\text{A17})$$

For finite CF, any scheme of this form passes through point C of Figure 15, and is therefore at least second-order accurate, as seen from equation (A14). If $CF = 1/8$, then the slope S is given by

$$S = 2CF + 0.5 = 0.75 \quad (\text{A18})$$

so that a steady-state control-volume scheme which passes through point C with a slope of $3/4$ is third-order accurate, according to equation (A16). Table I summarizes several second-order schemes in comparison with the third-order QUICK algorithm.

Table I.

Method	CF	S	Order
QUICK	1/8	3/4	Third
Eq. (A5)	1/6	5/6	Second
Fromm	1/4	1	Second
2nd-up	1/2	3/2	Second
Central	0	1/2	Second

APPENDIX II

Explicit control-volume time-marching algorithm

Using compass-point (plus 'top' and 'bottom') notation, fluxes are computed explicitly for the west, south and bottom faces. For example, for the west face

$$F_w = c_w \Phi_w - \alpha_w \text{GRAD}_w \quad (\text{A19})$$

where the west-face Courant number is

$$c_w = u_w \Delta t / \Delta x \quad (\text{A20})$$

and the corresponding diffusion parameter is

$$\alpha_w = D_w \Delta t / \Delta x^2 \quad (\text{A21})$$

The face-value is first computed explicitly, using (in general) a wide upwind-biased multidimensional stencil; then the universal-limiter constraints are applied—again explicitly—to give Φ_w . The gradient term is appropriately taken to be a second-order approximation simulating the diffusive flux; i.e.

$$\text{GRAD}_w = \left(\frac{\partial \Phi}{\partial x} \right)_w \Delta x = \Phi_p - \Phi_w \quad (\text{A22})$$

(A higher-order treatment of diffusion is not necessary because, for sharp changes in gradient, diffusion is very small, whereas when diffusion is large, gradients vary smoothly.) Then the update

algorithm consists of a FORTRAN over-write assignment statement inside a multiple DO-loop:

Set:

$$\begin{aligned}\Phi_p(i, j, k) = & \Phi_p(i, j, k) + F_w(i, j, k) + F_s(i, j, k) + F_b(i, j, k) \\ & - F_w(i+1, j, k) - F_s(i, j+1, k) - F_b(i, j, k+1) + \Delta t S(i, j, k)\end{aligned}\quad (\text{A23})$$

where conservation has been used—e.g. for the east face at (i, j, k) ,

$$F_e(i, j, k) = F_w(i+1, j, k) \quad (\text{A24})$$

and so on. Because of non-linearities inherent in the limiter, it is not possible to give precise stability restrictions on the time-step. However, experience suggests that local Courant numbers near 0.3 appear to give satisfactory results under high-convection conditions.

The steady-state limiter portrayed in Figure 15 needs to be slightly modified for the time-marching algorithm. Rather than using the *ad hoc* restriction given by OB, it is necessary to use a more precise condition corresponding to the time-accurate limiter,²⁹ i.e.

$$\tilde{\Phi}_f \leq \tilde{\Phi}_c / c \quad \text{for} \quad 0 \leq \tilde{\Phi}_c \leq 1 \quad (\text{A25})$$

(in addition to requiring $\tilde{\Phi}_f \leq 1$ in the same range) where c is the appropriate normal-direction Courant number at the CV face in question. Without this constraint, (very) slight undamped temporal oscillations may occur at isolated points near strong discontinuities at *finite* P_Δ values; at such points, a steady state might never be reached.

Although only first-order accurate in time, equation (A23) can give some indication of the temporal evolution of the solution from the assumed initial conditions. From a practical point of view, this can indicate the total time necessary for reaching a steady state. One simply observes how long it takes for initial transients near an upstream boundary to ‘wash out’ of a downstream boundary; then continued time-marching for 2 to 3 times this time-scale is usually enough to cause reflections and other transients to die away. Of course, more precise stopping criteria can easily be devised.

APPENDIX III

Higher-order multidimensional fluxes

For first- and second-order methods—including combinations such as Hybrid, EDS, PLDS and various TVD schemes—the multidimensional fluxes at each CV face are identical to their normal-direction one-dimensional counterparts. For second-order upwinding, for example, the left-face convective flux is given by upwind linear extrapolation in the normal direction,

$$\text{CFLUXL}(i, j, k) = \text{CXL}(1.5\Phi_{i-1, j, k} - 0.5\Phi_{i-2, j, k}) \quad (\text{A26})$$

where CXL is the appropriate left-face normal (x-component) Courant number. Note that, to a consistent order, no ‘transverse curvature’ terms are included.

At third order, it is appropriate to include transverse curvature; thus, for example, the QUICK left-face convective flux is given by

$$\text{CFLUXL}(i, j, k) = \text{CXL}\Phi_\ell^Q \quad (\text{A27})$$

where

$$\Phi_\ell^Q = \Phi_{\text{LIN}} - \frac{1}{8}\text{CURVNL} + \frac{1}{24}\text{CURVTL} \quad (\text{A28})$$

using the definition

$$\Phi_{\text{LIN}} = \frac{1}{2}(\Phi_{i,j,k} + \Phi_{i-1,j,k}) \quad (\text{A29})$$

and where, if $\text{CXL} \geq 0$, the normal and transverse ‘curvature’ terms are given by

$$\text{CURVNL} = (\Phi_{i,j,k} - 2\Phi_{i-1,j,k} + \Phi_{i-2,j,k}) \quad (\text{A30})$$

and

$$\begin{aligned} \text{CURVTL} = & (\Phi_{i-1,j+1,k} - 2\Phi_{i-1,j,k} + \Phi_{i-1,j-1,k}) \\ & + (\Phi_{i-1,j,k+1} - 2\Phi_{i-1,j,k} + \Phi_{i-1,j,k-1}) \end{aligned} \quad (\text{A31})$$

respectively; whereas, if $\text{CXL} < 0$,

$$\text{CURVNL} = (\Phi_{i+1,j,k} - 2\Phi_{i,j,k} + \Phi_{i-1,j,k}) \quad (\text{A32})$$

and

$$\begin{aligned} \text{CURVTL} = & (\Phi_{i,j+1,k} - 2\Phi_{i,j,k} + \Phi_{i,j-1,k}) \\ & + (\Phi_{i,j,k+1} - 2\Phi_{i,j,k} + \Phi_{i,j,k-1}) \end{aligned} \quad (\text{A33})$$

For higher-order convective fluxes, other transverse terms could be included. However, numerical experimentation has shown that

- (i) whereas inclusion of the third-order CURVT terms provides a significant increase in accuracy,
- (ii) higher-order transverse terms can actually reduce accuracy in some cases and are therefore omitted, and
- (iii) the coefficients of higher-order normal terms can be optimized to give better accuracy than that obtained from values using formal interpolation formulas.

Thus, for example, the ‘fifth-order’ convected value (at the left face) used in this paper is given by

$$\Phi_{\ell}^{(5)} = \Phi_{\text{LIN}} - \frac{1}{6}\text{CURVAV} + \frac{3}{128}\text{FOURTH} + \frac{1}{24}\text{CURVTL} \quad (\text{A34})$$

where CURVAV is an ‘average normal curvature’ across the left face

$$\text{CURVAV} = \frac{1}{2}(\Phi_{i+1,j,k} - \Phi_{i,j,k} - \Phi_{i-1,j,k} + \Phi_{i-2,j,k}) \quad (\text{A35})$$

FOURTH is the upwind-biased fourth-difference normal to the face

$$\text{FOURTH} = (\Phi_{i+1,j,k} - 4\Phi_{i,j,k} + 6\Phi_{i-1,j,k} - 4\Phi_{i-2,j,k} + \Phi_{i-3,j,k}) \quad (\text{A36})$$

(for $\text{CXL} > 0$), and CURVTL is as defined previously. Note the use of $1/6$ (rather than $1/8$) in equation (A34)!

The ‘seventh-order’ formula used in this paper is given by

$$\Phi_{\ell}^{(7)} = \Phi_{\text{LIN}} - \frac{1}{6}\text{CURVAV} + \frac{3}{128}\text{FRTHAV} + \frac{1}{100}\text{SIXTH} + \frac{1}{24}\text{CURVTL} \quad (\text{A37})$$

where FRTHAV is the (symmetrical) average fourth difference across the left face,

$$\text{FRTHAV} = (\Phi_{i+3} - 3\Phi_{i+2} + 2\Phi_{i+1} + 2\Phi_i - 3\Phi_{i-1} + \Phi_{i-2}) \quad (\text{A38})$$

(suppressing j ’s and k ’s), and SIXTH is the upwind-biased sixth difference normal to the face

$$\text{SIXTH} = (\Phi_{i+3} - 6\Phi_{i+2} + 15\Phi_{i+1} - 20\Phi_i + 15\Phi_{i-1} - 6\Phi_{i-2} + \Phi_{i-3}) \quad (\text{A39})$$

Formal interpolation would indicate factors of 1/8 multiplying CURVAV and 5/1024 multiplying SIXTH—together with additional transverse and cross-difference terms. The factors used in equation (A37) have been found to give slightly more accurate results.

In all cases, diffusive fluxes are modelled using the simple second-order approximation for the normal gradient. For example, for the left face,

$$\left(\frac{\partial \Phi}{\partial x}\right)_t = \frac{(\Phi_{i,j,k} - \Phi_{i-1,j,k})}{\Delta x} \quad (\text{A40})$$

As explained previously, higher-order terms are not warranted since, when diffusion is large, profiles are smooth and equation (A40) is consistent with the appropriate (QUICK) treatment of convection,¹³ whereas, when steep gradients occur—necessitating higher-order convective modelling and the use of the universal limiter—diffusion terms are very small, so that a simple diffusion model suffices.

REFERENCES

1. D. B. Spalding, 'A novel finite difference formulation for differential expressions involving both first and second derivatives', *Int. j. numer. methods eng.*, **4**, 551 (1972).
2. S. V. Patankar, *Numerical Heat Transfer and Fluid Flow*, Hemisphere Publishing, New York, 1980.
3. G. D. Raithby and G. E. Schneider, 'Elliptic systems: Finite-difference method II', in W. J. Minkowycz *et al.* (eds.), *Handbook of Numerical Heat Transfer*, Wiley, New York, 1988, p. 241.
4. G. deVahl Davis and G. D. Mallinson, 'An evaluation of upwind and central difference approximations by a study of recirculating flow', *Comp. Fluids*, **4**, 29 (1976).
5. B. P. Leonard, 'A consistency check for estimating truncation error due to upstream differencing', *Appl. Math. Modelling*, **2**, 239–244 (1978).
6. G. D. Raithby, 'A critical evaluation of upstream differencing applied to problems involving fluid flow', *Comp. Methods Appl. Mech. Eng.*, **9**, 75 (1976).
7. B. P. Leonard, 'A survey of finite differences with upwinding for numerical modelling of the incompressible convective diffusion equation', in C. Taylor and K. Morgan (eds.), *Computational Techniques in Transient and Turbulent Flow*, Vol. 2, Pineridge Press, Swansea, U.K., 1981, pp. 1–36.
8. P. G. Huang, B. E. Launder and M. A. Leschziner, 'Discretization of non-linear convection processes: A broad-range comparison of four schemes', *Comp. Methods Appl. Mech. Eng.*, **48**, 1 (1985).
9. M. A. Leschziner and W. Rodi, 'Calculation of annular and twin parallel jets using various discretization schemes and turbulence-model variants', *J. Fluids Eng. ASME*, **103**, 352–360 (1981).
10. S. A. Syed, L. M. Chiappetta and A. D. Gosman, 'Assessment of discretization schemes to reduce numerical diffusion in the calculation of complex flows', *AIAA Paper 85-0441* (1985).
11. A. D. Gosman and W. M. Pun, 'Calculation of recirculating flows', *Heat Transfer Section Report HTS/74/2*, Department of Mechanical Engineering, Imperial College, London, 1974.
12. M. A. Leschziner and K. P. Dimitriadis, 'Computation of three-dimensional turbulent flow in non-orthogonal junctions by a branch-coupling method', *Comp. Fluids*, **17**, 371–396 (1989).
13. B. P. Leonard, 'Elliptic systems: Finite difference method IV', Chapter 9 in W. J. Minkowicz *et al.* (eds.), *Handbook of Numerical Heat Transfer*, Wiley, New York, 1988, pp. 347–378.
14. C. Y. Perng and R. L. Street, 'Three-dimensional unsteady flow simulations: Alternative strategies for a volume-averaged calculation', *Int. j. numer. methods fluids*, **9**, 341–362 (1989).
15. J. R. Kossef, R. L. Street, P. M. Gresho, C. D. Upson, J. A. C. Humphrey and W. M. To, 'A three-dimensional lid-driven cavity flow: Experiment and simulation', *Proc. Third Int. Conf. on Numerical Methods in Laminar and Turbulent Flows*, Seattle, 1983, pp. 564–581.
16. P. H. Gaskell, A. K. C. Lau and N. G. Wright, 'Two efficient solution strategies for use with high order discretisation schemes, in the simulation of fluid flow problems', in C. Taylor *et al.* (eds.), *Numerical Methods in Laminar and Turbulent Flow*, Vol. 5, Pineridge Press, Swansea, 1987, p. 210.
17. C. J. Freitas, 'Non-linear transient phenomena in a three-dimensional cavity flow: A numerical investigation', *Ph.D. Dissertation*, Department of Civil Engineering, Stanford University, 1986.
18. G. D. Raithby, 'Skew-upstream differencing for problems involving fluid flow', *Comp. Methods Appl. Mech. Eng.*, **9**, 151 (1976).
19. J. Zhu and M. A. Leschnizer, 'A local oscillation-damping algorithm for higher-order convection schemes', *Comp. Methods Appl. Mech. Eng.*, **67**, 355–366 (1988).
20. A. Turan and J. P. VanDoormaal, 'Improved numerical methods for turbulent viscous recirculating flows', *NASA Contractor Report 180852*, Lewis Research Center, 1988.

21. P. D. Lax and B. Wendroff, 'Difference schemes with high order of accuracy for solving hyperbolic equations', *Commun. Pure Appl. Math.*, **17**, 381 (1964).
22. R. W. MacCormack, 'Effect of viscosity in hypervelocity impact cratering', *AIAA Paper*, 69-354 (1969).
23. A. Jameson and T. J. Baker, 'Euler calculations for a complete aircraft', *Proceedings of the Tenth International Conference on Numerical Methods in Fluid Dynamics (Lecture Notes in Physics, Vol. 264)*, Springer-Verlag, Berlin, 1986.
24. H. C. Yee, 'Upwind and symmetric shock-capturing schemes', *NASA TM-89464*, NASA-Ames Research Center, 1987.
25. P. K. Sweby, 'High resolution schemes using flux limiters for hyperbolic conservation laws', *SIAM J. Numer. Anal.*, **21**, 995 (1984).
26. P. L. Roe, 'Characteristic-based schemes for the Euler equations', in M. Van Dyke *et al.* (eds.), *Annual Reviews of Fluid Mechanics, Vol. 18*, Annual Reviews, New York, 1986, p. 337.
27. P. H. Gaskell and A. K. C. Lau, 'Curvature compensated convective transport: SMART, a new boundedness preserving transport algorithm', *Int. j. numer. methods fluids*, **8**, 617 (1988).
28. B. P. Leonard, 'Simple high accuracy resolution program for convective modelling of discontinuities', *Int. j. numer. methods fluids*, **8**, 901-927 (1988).
29. B. P. Leonard, 'Universal limiter for transient interpolation modeling of the advective transport equations: The ULTIMATE conservative difference scheme', *NASA TM 100916 (ICOMP-88-11)*, NASA-Lewis Research Center, 1988.
30. C. A. J. Fletcher, *Computational Techniques for Fluid Dynamics, Vol. I and II*, Springer-Verlag, Berlin, 1988.
31. J. C. Heinrich and O. C. Zienkiewicz, 'The finite element method and "upwinding" techniques in the numerical solution of convection dominated flow problems', in T. J. R. Hughes (ed.), *Finite Element Methods for Convection Dominated Flows*, AMD 34, ASME, New York, 1979, pp. 105-136.
32. R. G. Huguet, 'The evaluation and development of approximation schemes for the finite volume method', *Ph.D. Thesis*, University of Waterloo, 1985.
33. M. A. Leschziner, 'Practical evaluation of three finite difference schemes for the computation of steady-state recirculating flows', *Comp. Methods Appl. Mech. Eng.*, **23**, 293 (1980).
34. R. W. Lewis and K. Morgan (eds.), *Numerical Methods in Thermal Problems VI*, Pineridge Press, Swansea, U.K., 1989.
35. I. P. Castro and J. M. Jones, 'Studies in numerical computations of recirculating flows', *Int. j. numer. methods fluids*, **7**, 793 (1987).
36. R. F. Warming and R. M. Beam, 'Upwind second-order difference schemes and applications in aerodynamic flows', *AIAA J.*, **14**, 1241 (1976).
37. B. P. Leonard, 'A stable and accurate convective modelling procedure based on quadratic upstream interpolation', *Comp. Methods Appl. Mech. Eng.*, **19**, 59-98 (1979).
38. S. Mokhtari and B. P. Leonard, 'Analysis of oscillatory convection schemes', *Bull. Am. Phys. Soc.*, **32** (1987).
39. B. P. Leonard and H. S. Niknafs, 'Sharp monotonic resolution of discontinuities without clipping of narrow extrema', *Comp. Fluids*, to appear.
40. B. van Leer, 'Towards the ultimate conservative difference scheme. II. Monotonicity and conservation combined in a second-order scheme', *J. Comp. Phys.*, **14**, 361 (1974).
41. P. L. Roe, 'Some contribution to the modelling of discontinuous flows', in E. Engquist *et al.* (eds.), *Large Scale Computations in Fluid Mechanics, Part 2 (Lectures in Applied Mathematics 22)*, American Mathematical Society, 1985, p. 183.
42. S. K. Godunov, 'Finite difference method for numerical computation of discontinuous solutions of the equation of fluid dynamics', *Matematik Sbornik*, **47**, 271 (1959).
43. D. Bradley and M. Missaghi, 'A Taylor-series approach to numerical accuracy and third-order scheme for strong convective flows', *Comp. Methods Appl. Mech. Eng.*, **69**, 133-151 (1988).
44. J. E. Fromm, 'A method for reducing dispersion in convective difference schemes', *J. Comp. Phys.*, **3**, 176 (1968).